Constructing Co and Zn atomic pairs in core-shell Co_3S_4/NC@ZnS/NC derived from MOF-on-MOF nanostructures for enhanced photocatalytic CO_2 reduction to C_2H_4

Lili Huang [a], Shengpeng Mo [a,b,c,*], Xin Zhao [a], Jiangjing Zhou [a], Xiaobin Zhou [a], Yanan Zhang [a,**], Yinming Fan [a], Qinglin Xie [a], Bing Li [c], Junhua Li [b,**]

[a] College of Environment Science and Engineering, Guilin University of Technology, Guilin 541004, PR China
[b] State Key Joint Laboratory of Environment Simulation and Pollution Control, School of Environment, Tsinghua University, Beijing 100084, PR China
[c] Jiangsu Zhongchuang Qingyuan Technology Co., Ltd, Yancheng 224001, PR China

ABSTRACT

Herein, a core-shell structured Co_3S_4/NC@ZnS/NC heterojunction has been constructed via elaborately synthesizing metal-organic framework (MOF)-on-MOF precursors (ZIF-67@ZIF-8) and following controlled carbonization-sulfidation processes. The developed Co_3S_4/NC@ZnS/NC achieves higher performances for CO_2 photoreduction with water vapor towards CO (28.44 μmol g^{-1} h^{-1}), CH_4 (1.93 μmol g^{-1} h^{-1}) and C_2H_4 (12.23 μmol g^{-1} h^{-1}) in a continuous-flow condition under visible-light irradiation, which are significantly superior than those of Co_3S_4/NC and ZnS/NC. $^{13}CO_2$ isotope tracer analysis verifies that CO, CH_4 and C_2H_4 originate from the carbon source of CO_2. Experiments and DFT calculations confirm that constructing an electron transport layer (ZnS/NC) in Co_3S_4/NC@ZnS/NC can contribute to a feasible channel for the enhanced separation and transfer of charge carriers. In heterojunction, non-bonding Co and Zn atomic pairs as adsorption sites synergistically participate in the CO_2 activation through the unique electron transport channel and acquire the lower energy barriers of COOH* formation. Moreover, in situ DRIFTS reveals the key intermediates and possible conversion pathways to main products. This work presents an attractive strategy to construct dual MOFs-derived metal sulfide heterojunctions for high-performance CO_2 conversion.

1. Introduction

The excessive atmospheric carbon dioxide (CO_2) emission derived from the huge consumption of fossil fuels has resulted in adverse environmental consequences such as ocean acidification and global warming [1]. To mitigate rising CO_2 levels in the atmosphere, numerous efforts have been devoted to carbon capture, storage and utilization [2]. Thereinto, the conversion of CO_2 towards valuable fuels through solar energy is proposed as a win-win strategy to simultaneously alleviate the environmental crises and create renewable carbon cycles [3,4]. In particular, C2 products (such as C_2H_4) have garnered interest because of their high energy content and application values [5]. Nevertheless, the photoreduction CO_2 coupled with H_2O to C_2H_4 still suffers from low conversion efficiencies and dissatisfactory products owing to the high CO_2 activation energy and multiple complex processes [5,6].

Consequently, the design and synthesis of photocatalysts for achieving high-efficiency CO_2 conversion and utilization remains an urgent task.

Typically, the process of CO_2 photoreduction mainly contains the light absorption, separation and transfer of photogenerated charge carriers, as well as the adsorption and activation of CO_2 [7]. Current research focuses on developing various photocatalytic materials to enhance the above three principal steps [7]. Among them, metal sulfides (such as Co_9S_8 [8], $ZnIn_2S_4$ [9], SnS_2 [10]) exhibit appropriate energy band structure, wide visible light response and unique electronic structure, which contribute to the photocatalytic conversion of CO_2 into valuable chemicals. However, it is undeniable that the photocatalytic activity can hardly be improved because of the rapid recombination rate of photogenerated carriers in a single-component catalyst [1]. As a result, various strategies including surface modification [11], co-catalysts introduction [12], morphology regulation [13], and

---

heterojunction construction [14] are adopted to boost photocatalytic performances. Specially, the coupling of two or more matched metal sulfides forming a heterojunction to create an internal built-in electric field is deemed as one of the most promising methods to powerfully improve the transport of photogenerated electron-hole pairs [15,16]. Meanwhile, the metal sulfide hybrids also possess increased potential catalytic sites and improved photo-stability compared with their individual counterparts [1,17]. Moreover, the introduction of carbon matrix to the photocatalyst can provide superior light absorption capacity and high conductivity for further enhancing the photocatalytic efficiency [18,19]. In this regard, it is highly desirable to fabricate an efficient metal sulfide heterojunction with carbon matrix to obtain excellent photocatalytic performances during the CO_2 reduction reaction.

In recent years, metal-organic frameworks (MOFs) consisting of metal ions/clusters interconnected with organic ligands have been identified as promising precursors for developing functional materials with specific physicochemical properties [20]. In view of the physicochemical versatility and structural adjustability of a single MOF, controllable integration of two or more different MOFs towards MOF-on-MOF composites can provide a new approach to transform into core-shell precursors [21]. In general, the synthetic strategy of MOF-on-MOF involves the epitaxial growth with matched lattices or mismatched lattices. According to previous studies, core-shell precursors of ZIF-8@ZIF-67 [22], UiO-66-N@x-ZIF-67 [23] and MIL-88A@ZIF-8@ZIF-67 [24] have been successfully prepared. When MOF precursors are pyrolyzed under an inert atmosphere, the metal sites in core-shell nanostructures can remain stable and uniform with the presence of carbon matrix [25]. Notably, Zhu et al. developed a novel $Cu_9S_5/NC@Co_3S_4/NC$ core-shell material derived from $Cu_3(BTC)_2@$-ZIF-67 through facile carbonization and sulfidation processes, which verified that the conversion of dual MOFs precursors into carbon-based metal sulfide heterojunction was feasible [26]. Additionally, heterojunction materials obtained from core-shell MOF-on-MOF composites can build high-quality interfaces due to their large area of intimate interface contact, thus achieving efficient interfacial charge separation/transfer [25]. However, whether the construction of a special electron transport interface in these core-shell materials can enhance the photocatalytic performance of CO_2 reduction?

Accordingly, we elaborately constructed a core-shell ZIF-67@ZIF-8 by adopting the MOF-on-MOF strategy, which was achieved by the epitaxial growth of ZIF-8 layer along ZIF-67 crystal nuclei. Then, the ZIF-67@ZIF-8 precursors were subjected to controlled pyrolysis and sulfidation treatments, producing a heterojunction catalyst with core-shell distributed Co_3S_4 and ZnS nanoparticles embedded within nitrogen-doped carbon skeletons (NC) (denoted as $Co_3S_4/NC@ZnS/NC$). Due to the unique composition and structural merits, $Co_3S_4/NC@ZnS/NC$ demonstrates enhanced CO_2 adsorption and excellent visible light absorption ability. Impressively, the formation of ZnS/NC in the core-shell heterojunction acts as an electron transport layer, which can regulate the electronic structure and promote the separation and transfer of carriers. As a consequence, under visible-light irradiation, the $Co_3S_4/NC@ZnS/NC$ exhibits the efficient conversion of CO_2 with water vapor towards CO, CH_4 and C_2H_4, which significantly exceed those of Co_3S_4/NC and ZnS/NC. In addition, the interface charge transfer process and possible chemical reaction path are illustrated via DFT calculations and in situ DRIFTS, respectively.

2. Experimental section

2.1. Materials

Cobaltous nitrate hexahydrate ($Co(NO_3)_2 \cdot 6H_2O$), Zinc nitrate hexahydrate ($Zn(NO_3)_2 \cdot 6H_2O$), 2-methylimidazole, polyvinylpyrrolidone (PVP, K29–32, Mw~58000) and thioacetamide were bought from Aladdin. Methanol (CH_3OH) was bought from Xilong Scientific Co., Ltd. All reagents were analytical reagent grade and without further

purification.

2.2. Catalysts preparation

2.2.1. Synthesis of ZIF-67

First, 12.5 mmol $Co(NO_3)_2 \cdot 6H_2O$ and 75.0 mmol 2-methylimidazole (2-MeIm) were dissolved in 150 mL methanol, respectively. Next, the solution of 2-MeIm was quickly injected into the $Co(NO_3)_2 \cdot 6H_2O$ solution. The mixture was stirred for 30 min and kept at room temperature for 24 h. Finally, the purple precipitates were acquired after centrifugation, washed with methanol and dried at 60 °C for 12 h.

2.2.2. Synthesis of ZIF-8

Typically, 20 mmol $Zn(NO_3)_2 \cdot 6H_2O$ and 120 mmol 2-MeIm were dissolved in 150 mL methanol, respectively. Then, the latter solution was poured into the former solution to form a mixed solution. After continuous stirring at room temperature for 24 h, centrifuged, and washed several times with methanol to obtain a white precipitate. The next step was to dry the sample at 60 °C overnight to obtain the target product.

2.2.3. Synthesis of ZIF-67@ZIF-8

200 mg ZIF-67 powder and 0.5 g PVP were ultrasonically dispersed in 15 mL methanol. The obtained dispersion was continuously stirred for 12 h at room temperature, then centrifuged and rinsed several times with methanol. Subsequently, the PVP-functionalized ZIF-67 and X mmol $Zn(NO_3)_2 \cdot 6H_2O$ (X=0.50, 0.75 and 1.0) were added into a 15 mL methanol solution and stirred for 30 min at room temperature. Next, a mixture containing 4 mmol of 2-MeIm and 15 mL of methanol was added dropwise into the above-mentioned solution and maintained stirring for 2 h. The resulting ZIF-67@ZIF-8 precursors were collected via centrifugation and washed thoroughly with methanol, and finally dried at 60 °C overnight.

2.2.4. Synthesis of CoO_x/NC, ZnO/NC, $CoO_x/NC@ZnO/NC$

In brief, the ZIF-67, ZIF-8 and ZIF-67@ZIF-8 precursors were pyrolyzed at 550 °C for 2 h with a heating rate of 2 °C min^{-1} under continuous N_2 flow, resulting in corresponding $CoO_x@NC$, ZnO/NC and $CoO_x/NC@ZnO/NC$. $CoO_x/NC@ZnO/NC$ samples obtained from 0.50, 0.75, and 1.0 mmol of Zn amounts were labeled $CoO_x/NC@ZnO/NC$ (0.5), $CoO_x/NC@ZnO/NC$ and $CoO_x/NC@ZnO/NC$ (1.0), respectively.

2.2.5. Synthesis of Co_3S_4/NC, ZnS/NC, $Co_3S_4/NC@ZnS/NC$

In a typical synthesis, the CoO_x/NC (100 mg) and thioacetamide (TAA, 100 mg) were put into 30 mL deionized (DI) water and stirred uniformly, which were then transferred to a 50 mL Teflon-lined stainless steel autoclave and solvothermal treatment at 160 °C for 8 h. Then, the sample was collected by centrifugation and washed repeatedly with ethanol and DI water, and finally dried at 60 °C for 8 h to yield Co_3S_4/NC products. The ZnS/NC, $Co_3S_4/NC@ZnS/NC$ (0.5), $Co_3S_4/NC@ZnS/NC$ and $Co_3S_4/NC@ZnS/NC$ (1.0) were obtained via the same sulfidation process using ZnO/NC, $CoO_x/NC@ZnO/NC$ (0.5), $CoO_x/NC@ZnO/NC$ and $CoO_x/NC@ZnO/NC$ (1.0) as reactants, respectively.

2.3. Characterization

X-ray diffraction (PXRD) patterns of samples were determined using a Panalytical X'Pert PRO X-ray diffractometer with Cu-Kα radiation (λ = 1.5406 Å) at 40 kV and 40 mA. The morphology was measured via a field emission scanning electron microscope (FESEM, JEOL JSM-6700 F) at 15 kV and a transmission electron microscopy (TEM, JEOL JEM-2100 F) at 200 kV. Raman spectra were carried out on a Horiba Scientific LabRAM Raman NSOM under an excitation wavelength of 532 nm. X-ray photoelectron spectroscopy (XPS) was performed on Thermo Fisher Scientific ESCALAB250Xi photoelectron spectrometer and the binding energies were corrected with reference to C 1 s peak at 284.6 eV. The

surface areas, pore size distributions and CO_2 adsorption isotherms were obtained by means of a Micromeritics ASAP 2020 analyzer, CO_2 temperature programmed desorption (CO_2–TPD) measurements were performed on a chemisorption analyzer (AutoChem II 2920, Micromeritics). UV–visible diffuse reflectance spectra (UV–vis DRS) of the powder samples were conducted by a Shimadzu UV-2550 spectrophotometer with the white $BaSO_4$ used as reference. Steady-state photoluminescence (PL) spectra were acquired from an Edinburgh FLS1000 spectrofluorometer at room temperature. Electron paramagnetic resonance (EPR) spectra were measured by an A300 Bruker spectrometer at room temperature. The ^{13}C isotope test was conducted by gas chromatography-mass spectrometry (GC-MS, Shimadzu QP2010 Plus). Using inductively coupled plasma optical emission spectrometry (Agilent 725 ICP-OES) to determine the Co, Zn contents.

2.4. Photoelectrochemical tests

The electrochemical measurements were carried out using a CHI 660E electrochemical workstation (Shanghai Chenhua, China) with a standard three-electrode system in 0.5 mol L^{-1} Na_2SO_4 solution and a 300 W Xe lamp ($\lambda > 420$ nm) was used as the light source. A Pt wire and an Ag/AgCl electrode served as the counter and reference electrodes, respectively. The FTO glass was dip-coated with photocatalysts used as the work electrode. The electrochemical impedance spectroscopy (EIS) was recorded in the frequency range of 0.01–10^5 Hz and Mott-Schottky tests were performed at different frequencies (750 Hz, 1000 Hz).

2.5. In situ DRIFTS tests

In situ DRIFTS tests were performed using a Nicolet 6700 spectrometer (Thermo Fisher Scientific, USA). Before catalytic testing, the sample was loaded in the center of the cell and pretreated in N_2 atmosphere at 150 °C for 30 min. When the reaction cell cooled down to room temperature, the background spectrum was recorded. Then, a mixture of CO_2 and water vapor was injected into the reactor. After achieving adsorption equilibrium, light irradiation (300 W Xe lamp, $\lambda > 420$ nm) was introduced into the reaction space and the IR signals were recorded in real time over the entire test process.

2.6. Photocatalytic activity evaluation

The photocatalytic reaction was conducted in a 200 mL steady-flow dynamic reactor made from stainless steel with a 42 mm diameter quartz-glass window at the top. The 35 mg photocatalyst was added into 2.0 mL ethanol and formed a homogeneous dispersion, and then slowly dripped onto the 42 mm diameter fiberglass filter. After drying, the piece of the filter was transferred to the reactor and 50 mL min^{-1} of high-purity CO_2 (99.99%) was added to the reactor for 30 min to achieve complete air purification. Subsequently, high-purity CO_2 gas (3 mL min^{-1}) was continuously introduced into a bubbler containing 200 mL deionized water at a controlled temperature of 25 °C. A 300 W Xenon lamp with a UV-light cut-off filter ($\lambda > 420$ nm) was employed as the light source with an illumination intensity of 920 mW cm^{-2}. The reaction products were collected every 10 min during the irradiation process and analyzed online using a gas chromatography (GC, Shanghai Fan-Wei GC-6600).

The selectivity of CO, CH_4 and C_2H_4 was obtained by the following equations:

$$CO \text{ selectivity} = [2n(CO)]/[2n(CO) + 8n(CH_4) + 12n(C_2H_4)] \times 100\%$$
$$(1)$$

$$CH_4 \text{ selectivity} = [8n(CH_4)]/[2n(CO) + 8n(CH_4) + 12n(C_2H_4)] \times 100\%$$
$$(2)$$

$$C_2H_4 \text{ selectivity} = [12n(C_2H_4)]/[2n(CO) + 8n(CH_4) + 12n(C_2H_4)] \times 100\%$$
$$(3)$$

where n represents the yield of corresponding product.

2.7. Theoretical calculations

All the calculations were performed according to spin-polarized density functional theory (DFT) route, implemented by Vienna Ab-initio Simulation Package (VASP) with projector augmented wave (PAW) pseudopotential to tackle the electron-ion interactions. The exchange and correlation functional were treated with Perdew Burke-Ernzerhof (GGA-PBE) generalized gradient approximation. The cutoff energy was set as 400 eV and convergence criteria were set to 10^{-4} eV for the energy and -0.01 eV/Å for the force. The k-point meshes were set of $2 \times 3 \times 1$ and $3 \times 3 \times 1$ for geometry optimization and electronic self-consistent, respectively. The adsorption energy (E_{ads}) is defined by: $E_{ads} = E_{total} - E_{surface} - E_{gas}$, where E_{total}, $E_{surface}$ and E_{gas} correspond to the energy of the entire system, the empty catalyst surface and the individual CO_2 molecule, respectively. A negative E_{ads} means a higher adsorption capacity. The change of the Gibbs free energy (ΔG) for each step can be written as: $\Delta G = \Delta E + \Delta ZPE - T\Delta S$, where ΔE is the energy that can be directly acquired from the DFT calculations, ΔZPE represents zero-point energy correction. T is the reaction temperature which is set to 298.15 K in this study and ΔS represents the change in entropy.

3. Results and discussion

3.1. Structural characterization and surface properties

The synthetic process of Co_3S_4/NC@ZnS/NC heterojunction derived from dual MOFs is briefly illustrated in Fig. 1a. The formation process involved epitaxial growth, carbonization and sulfidation. First of all, the ZIF-67 rhombic dodecahedrons were prepared via a precipitation method. Subsequently, the core-shell solid ZIF-67@ZIF-8 was successfully fabricated by epitaxial growth of a ZIF-8 layer on the surface of ZIF-67 nanocrystals. Then, ZIF-67@ZIF-8 was transformed into a CoO_x/NC@ZnO/NC sample after carbonization treatments. Finally, the Co_3S_4/NC@ZnS/NC heterojunction with core-shell distributed Co_3S_4 and ZnS nanoparticles was obtained by the sulfidation reaction containing the sulfur source of thioacetamide (TAA). ICP-OES analysis shows that the Co/Zn ratio in the optimal Co_3S_4/NC@ZnS/NC is 2.78, which is similar to ZIF-67@ZIF-8 (3.19) and CoO_x/NC@ZnO/NC (2.92) (Table S1).

Aiming to study the morphological evolution of samples at various stages, FESEM technique was conducted. The pure ZIF-67 exhibits a well-defined rhombic dodecahedral structure with an average particle size measured as about 436 nm (Fig. 1b, f). Obviously, the morphology of ZIF-67@ZIF-8 is similar to that of ZIF-67 except for a slight increase in particle size (465 nm), indicating a thin ZIF-8 layer has been successfully grown on the host MOF surface (Fig. 1c, g). Besides, the pure ZIF-8 also exhibits a rhombic dodecahedral structure, which agrees with previous reports [22] (Fig. S1a). After pyrolysis treatment, the as-obtained CoO_x/NC retains the rhombic dodecahedral, but its surface shrinks and the size decreases from 436 to 393 nm (Fig. S2). CoO_x/NC@ZnO/NC also has a well-inherit dodecahedral structure with rough external surfaces and an average particle size is around 398 nm (Fig. 1d, h). Compared with CoO_x/NC, the surface shrinkage of CoO_x/NC@ZnO/NC is relatively low, which can be attributed to the well-preserved surface morphology of ZIF-8 during the pyrolysis process under an inert atmosphere [27] (Fig. S1b). With further sulfidation treatment, the as-obtained Co_3S_4/NC reveals severe surface shrinkage and a reduction in size (from 393 to 359 nm), leading to the formation of irregular shapes (Fig. S3). The ZnS/NC basically maintains the polyhedral shape but with the coarsened surfaces (Fig. S1c). In addition, the final formation of Co_3S_4/NC@ZnS/NC presents an indistinct dodecahedron
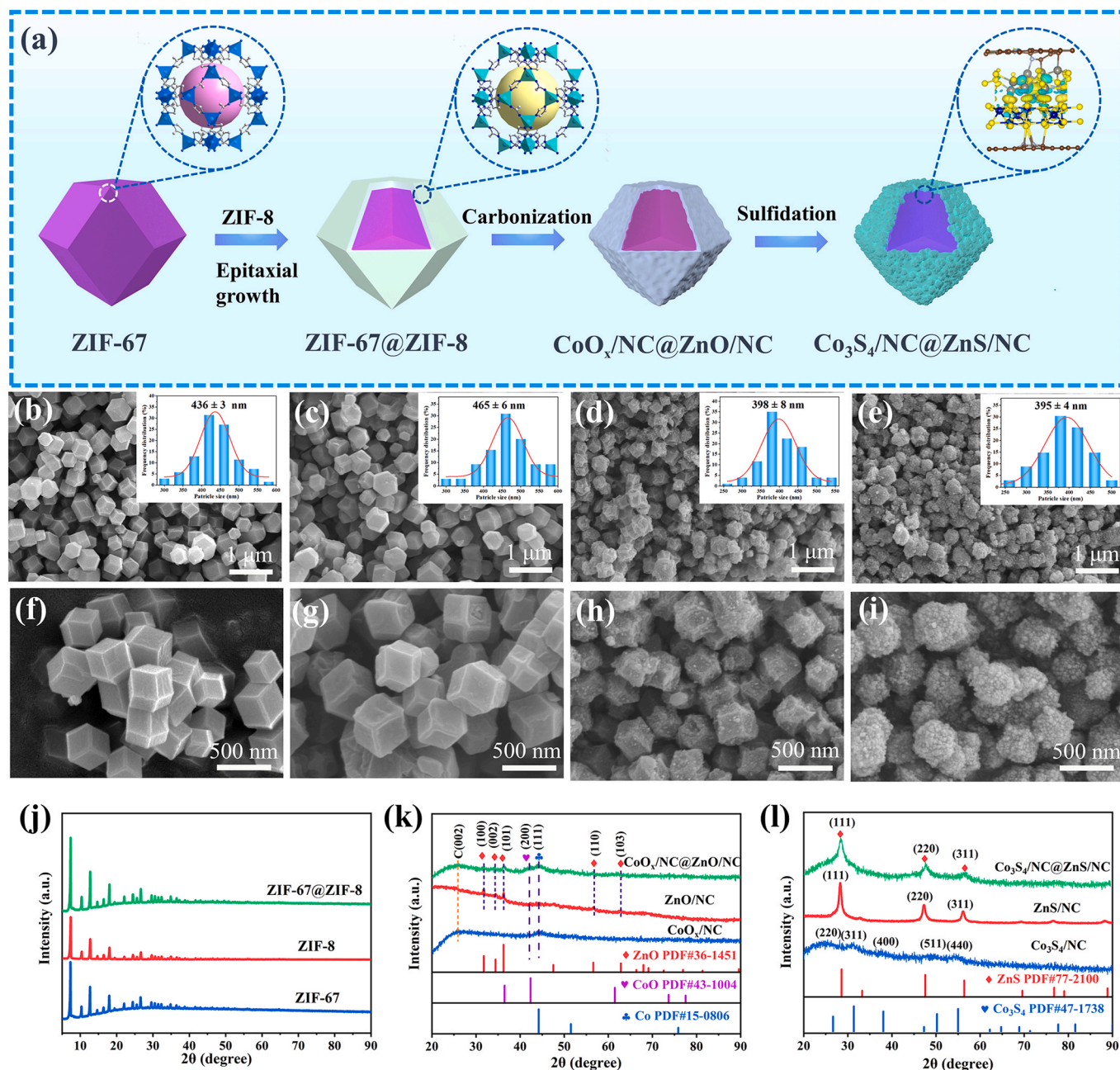
Fig. 1. (a) Scheme for preparation of Co$_3$S$_4$/NC@ZnS/NC composite, SEM images of (b, f) ZIF-67, (c, g) ZIF-67@ZIF-8, (d, h) CoO$_x$/NC@ZnO/NC and (e, i) Co$_3$S$_4$/NC@ZnS/NC, XRD patterns of different samples: (j) ZIF-67, ZIF-8 and ZIF-67@ZIF-8, (k) CoO$_x$/NC, ZnO/NC and CoO$_x$/NC@ZnO/NC, (l) Co$_3$S$_4$/NC, ZnS/NC and Co$_3$S$_4$/NC@ZnS/NC.

structure with a slight shrinkage in particle size (395 nm) (Fig. 1e, i). It is noteworthy that the surface of Co$_3$S$_4$/NC@ZnS/NC appears to be composed of continuous nanoparticles, which is related to the inconsistent shrinkage degree of individual components and the formation of ZnS.

Furthermore, the phases and crystalline structures of these as-obtained samples were confirmed by XRD measurement. As depicted in Fig. 1j, both ZIF-67 and ZIF-8 show a series of sharp diffraction peaks, which match well with the standard patterns of ZIF-67 and ZIF-8 [28]. The diffraction pattern of ZIF-67@ZIF-8 is virtually identical to that of ZIF-8 and ZIF-67 on account of isostructural topologies of ZIF-67 and ZIF-8. The diffraction peaks of the precursors disappear in the carbonized samples, suggesting that the phase transition is complete after pyrolysis (Fig. 1k). As shown in the XRD pattern of CoO$_x$/NC, two peaks

around 42.3° and 44.2° correspond to the (200) plane of CoO (JCPDS No. 43–1004) and the (111) plane of metallic Co (JCPDS No.15–0806) [29,30], respectively. In addition, the diffraction peak at 25.8° is indexed to graphitic carbon, because the existence of the Co species (Co^0, CoO) in carbonized ZIF-67 promotes the conversion of amorphous carbon to graphitized carbon [30]. As for ZnO/NC, the diffraction peaks are in good accordance with the crystal planes of ZnO (JCPDS No.36–1451) [31]. The relevant XRD patterns show that the low-temperature treatment of ZIF-8 leads to low crystallinity of ZnO and low graphitization degree [27]. Meanwhile, the carbonized sample of ZIF-67@ZIF-8 displays complex diffraction patterns, which are assigned to the crystal planes of Co species (Co^0, CoO) and ZnO. This verifies the successful epitaxial growth of ZIF-8 on the ZIF-67 surface. After the sulfidation treatment of CoO$_x$/NC (Fig. 1l), the weak diffraction peaks of

the corresponding product are consistent with crystal planes of Co_3S_4 [32] (JCPDS No. 47–1738). The ZnS/NC (Fig. 1l) from the sulfidation of ZnO/NC shows distinct diffraction peaks, which are indexed to the cubic structure of ZnS (JCPDS No. 77–2100) [33]. By observation, the XRD pattern of Co_3S_4/NC@ZnS/NC shows obvious diffraction peaks similar to those of ZnS/NC but no diffraction peaks belonging to Co_3S_4/NC are discovered (Fig. 1l). This might be due to the poor crystallinity of

Co_3S_4/NC being covered by diffraction peaks of the outer layer ZnS/NC.

More detailed structure features of the above-fabricated samples were revealed by TEM characterization. In Fig. S4a, ZIF-67@ZIF-8 shows a dodecahedron shape with smooth surfaces. The core-shell ZIF-67@ZIF-8 is verified by elemental mapping images, where Co is distributed on the core and Zn on the shell (Fig. S4b-f). As displayed in Figs. 2a, b and S5, the CoO_x/NC demonstrates regular polyhedral
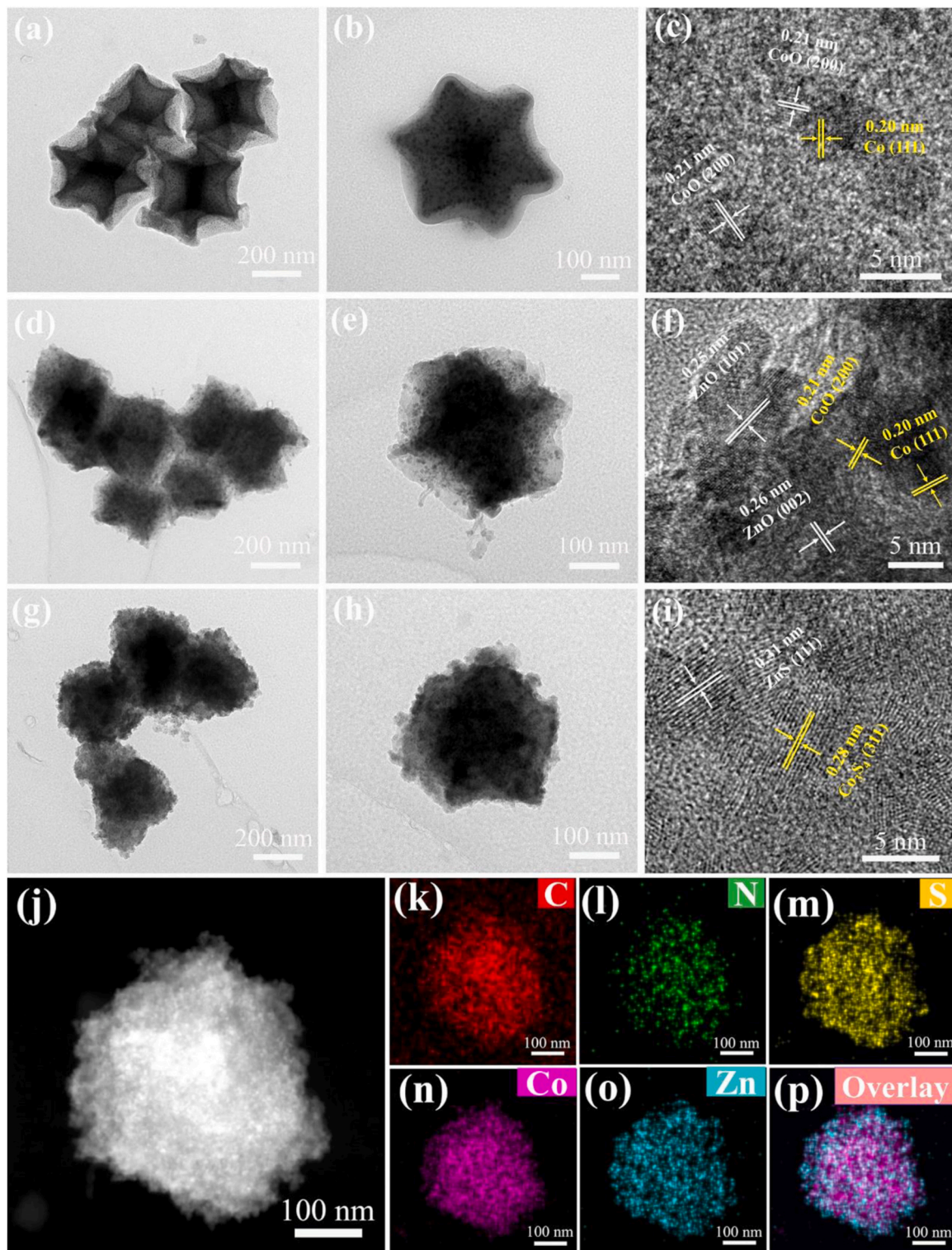

Fig. 2. TEM and HRTEM images of (a-c) CoO_x/NC, (d-f) CoO_x/NC@ZnO/NC and (g-i) Co_3S_4/NC@ZnS/NC, (j-p) elemental mapping images of Co_3S_4/NC@ZnS/NC for C, N, S, Co and Zn elements.

structures with obvious surface shrinkage, and small Co species nanoparticles are highly dispersed in the carbon matrix. According to the HRTEM image (Fig. 2c), two lattice fringe distances of 0.20 nm and 0.21 nm are observed, which are attributed to the (111) plane of metallic Co and the (200) plane of CoO [30,34], respectively. Actually, it is difficult to distinguish the above two lattice plane information, because the lattice fringe distances are too close. As for CoO_x/NC@ZnO/NC, the TEM images confirm that the embedded ZnO nanoparticles in the outer carbon matrix can protect the structure stability from surface rapid shrinkage (Fig. 2d, e). The HRTEM image (Fig. 2f) further reveals that in addition to the lattice fringes corresponding to CoO_x, the lattice fringe distances of 0.25 and 0.26 nm can be ascribed to the (101) and (002) planes of ZnO, respectively [31]. Moreover, the elemental mapping images of CoO_x/NC@ZnO/NC indicate the Co element is distributed in the core, which is completely covered by Zn element (Fig. S6). The TEM image of Co_3S_4/NC exhibits a relatively irregular polyhedral structure because the carbon matrix of CoO_x/NC is not sufficient to withstand the etching of sulfur during the hydrothermal sulfidation process (Fig. S7a, b). Compared with CoO_x/NC, the distribution of Co_3S_4 nanoparticles in the carbon matrix is denser (Fig. S7c). It can be seen from Fig. S7d, the distinct lattice fringe at 0.28 nm is indexed to the (311) crystal planes of Co_3S_4 [32], which is in agreement with the XRD results. From the TEM images of Fig. 2g and h, the Co_3S_4/NC@ZnS/NC displays a polyhedral structure with an indistinct outline and fluffy surface. The HRTEM image of Fig. 2i demonstrates the presence of interlaced lattice distances at about 0.28 and 0.31 nm, which can be assigned to the (311) crystal planes of Co_3S_4 [32] and (111) crystal planes of ZnS [17], respectively. This directly indicates the formation of heterointerface in Co_3S_4/NC@ZnS/NC. According to the energy dispersive spectrometer (EDS) analysis (Fig. S8a), the elements of C, N, Co, Zn and S co-exist in Co_3S_4/NC@ZnS/NC, meaning the successful introduction of sulfur element into the composite. Besides, the elemental mapping images (Fig. 2j-p) and elemental line-scanning profile

(Fig. S8b) show the Zn species are uniformly coated on the inner core of Co species, which suggests the core-shell structure of Co_3S_4/NC@ZnS/NC.

The composition and chemical state of these samples at each stage were analyzed by XPS spectra. In the Co 2p spectrum of CoO_x/NC (Fig. 3a), two peaks at 778.0 and 794.9 eV are identified as the $2p_{3/2}$ and $2p_{1/2}$ of Co^0, respectively, and two peaks at 781.2 and 796.8 eV belong to $2p_{3/2}$ and $2p_{1/2}$ of Co^{2+}, respectively [34]. Obviously, there are only slight shifts in the binding energies of the four peaks at CoO_x/NC@ZnO/NC compared to those of CoO_x/NC, indicating that the ZnO/NC coating on the CoO_x/NC can maintain the valence state of Co species well. It is not difficult to find that the binding energies of Co species significantly change after the sulfidation reaction. For Co_3S_4/NC (Fig. 3b), the Co^{3+} $2p_{3/2}$ and Co^{3+} $2p_{1/2}$ doublets are situated at 779.1 and 794.6 eV, respectively, while the peaks located at 782.1 and 798.3 eV are attributed to the respective Co^{2+} $2p_{3/2}$ and Co^{2+} $2p_{1/2}$ [32]. Moreover, the remaining two peaks at 786.4 and 803.6 eV are assigned to their relevant satellite peaks. The Zn 2p spectrum of ZnS/NC (Fig. 3c) reveals two clear peaks at 1021.9 and 1044.9 eV could be indexed to Zn $2p_{3/2}$ and Zn $2p_{1/2}$ [28]. Attentively, the binding energies of Co 2p in Co_3S_4/NC@ZnS/NC shift towards a higher position compared to Co_3S_4/NC, whereas Zn 2p in Co_3S_4/NC@ZnS/NC shift to lower binding energy values relative to ZnS/NC. Such shifts indicate that the charge transfer occurs between Co_3S_4/NC and ZnS/NC, which can effectively facilitate the formation of the internal electric field at interfaces [35]. The well-fitted three peaks at 284.6, 286.3 and 288.6 eV in the C 1s spectrum of Co_3S_4/NC (Fig. 3d) correspond to C−C, C−N/C−O, and O−C═O, respectively. Furthermore, the N 1s spectrum of CoO_x/NC (Fig. S9) can be divided into three prominent peaks at 398.0, 398.8 and 400.4 eV, which are related to pyridinic-N, pyrrolic-N, and graphitic-N, respectively [36]. The higher percentage of graphitic-N in Co_3S_4/NC and Co_3S_4/NC@ZnS/NC than that in CoO_x and CoO_x/NC@ZnO/NC indicates that the sulfidation process could change
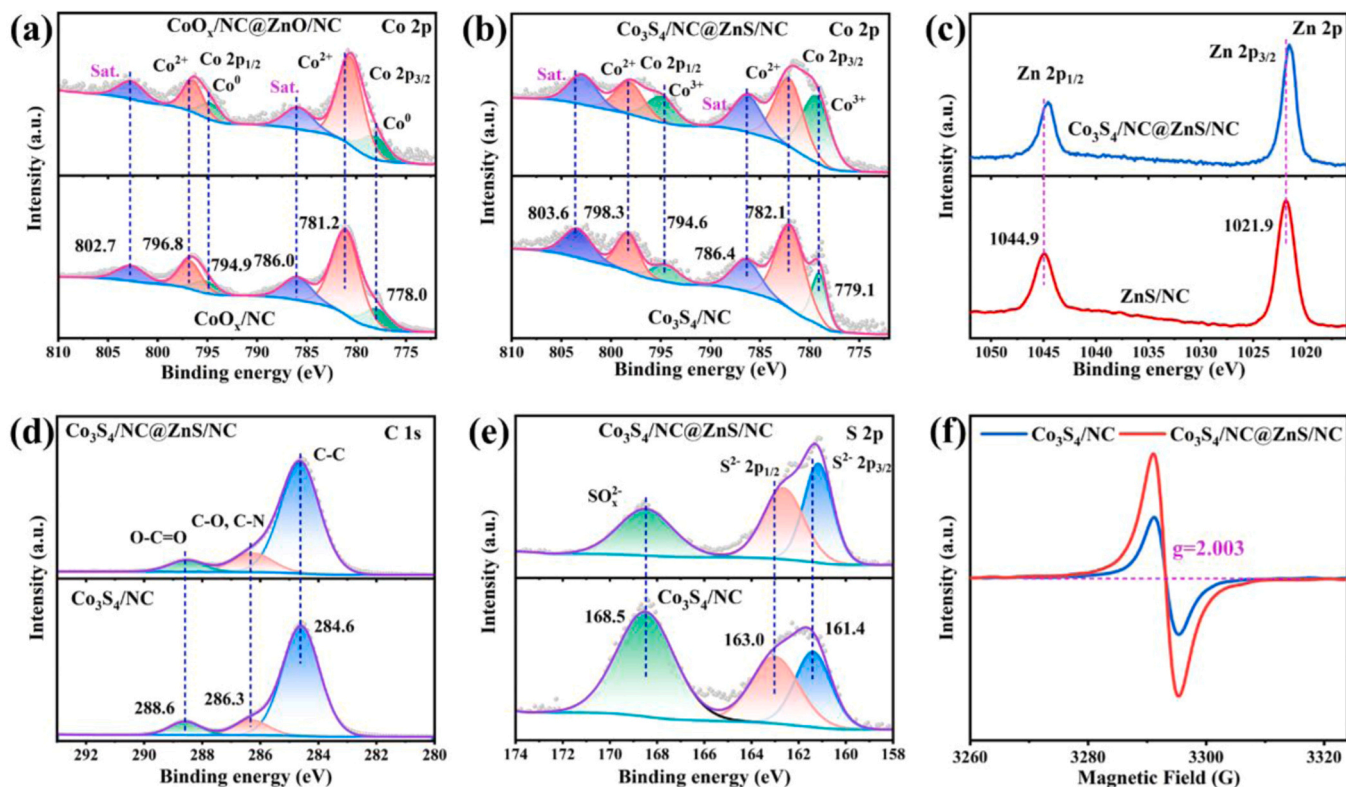

Fig. 3. High-resolution XPS spectra of (a, b) Co 2p, (c) Zn 2p, (d) C 1s, (e) S 2p of various samples, (f) EPR signal of S vacancies for Co_3S_4/NC and Co_3S_4/NC@ZnS/NC.

the properties of N species, thus enhancing the electrical conductivity of these samples [37,38]. As for S 2p, three peaks located at 161.4, 163.0 and 168.5 eV are detected in Co_3S_4/NC (Fig. 3e), which are attributable to S^{2-} $2p_{3/2}$, S^{2-} $2p_{1/2}$ and surface oxidation sulfur species (SO_x^{2-}), respectively [32]. In contrast to Co_3S_4/NC, the binding energies of S 2p in Co_3S_4/NC@ZnS/NC exhibit negative shifts, suggesting that there is a higher concentration of sulfur vacancies in Co_3S_4/NC@ZnS/NC due to the lower coordination of sulfur atoms [39,40]. To confirm this, the EPR test was performed. As presented in Fig. 3f, a typical EPR signal at g = 2.003 is detected in Co_3S_4/NC, owing to the unpaired electrons trapped around the sulfur vacancies [41]. Obviously, Co_3S_4/NC@ZnS/NC displays a higher signal intensity than the Co_3S_4/NC, which implies a higher concentration of S vacancies in Co_3S_4/NC@ZnS/NC. In general, abundant S vacancies could play a positive role in the absorption of CO_2 molecules and separation of photogenerated carriers [42,43].

3.2. Photocatalytic performance of catalysts

The photocatalytic CO_2 reduction activities of all photocatalysts were evaluated in a continuous flow reaction system just using water vapor and CO_2 as feedstocks. The reaction products were analyzed every 10 min under light irradiation ($\lambda \geq 420$ nm). As uncovered in Fig. 4a-c and S10a-c, the major products of photocatalytic system are CO and C_2H_4, while a small amount of CH_4 is also detected. The photocatalytic performance of all photocatalysts gradually tends to stabilize after 3.5 h of continuous reaction. The CoO_x/NC@ZnO/NC presents relatively higher generation rates for CO (17.19 μmol g^{-1} h^{-1}) and C_2H_4 (4.39 μmol g^{-1} h^{-1}) after stabilization, which are 1.55 and 1.69 times higher than that of CoO_x/NC, respectively, as well as 1.98 and 1.50 times higher than that of ZnO/NC, respectively (Fig. S11a). Besides, more CH_4 is generated on CoO_x/NC@ZnO/NC than on CoO_x/NC and ZnO/NC. As expected, all the Co_3S_4/NC@ZnS/NC samples show remarkably enhanced photocatalytic activity compared to Co_3S_4/NC and ZnS/NC (Figs. 4d and S10). Specifically, the production rates of CO, CH_4 and C_2H_4 over the optimal Co_3S_4/NC@ZnS/NC (Zn amount is 0.75 mmol) can reach 28.44, 1.93 and 12.23 μmol g^{-1} h^{-1}, which are 1.48, 1.08 and

1.43 times higher than those of Co_3S_4/NC, respectively. Meanwhile, the production rates of all reaction products for Co_3S_4/NC are superior to those of ZnS/NC in the same conditions. Noteworthily, it is demonstrated that the CO_2 photoreduction performance of Co_3S_4/NC and ZnS/NC is higher than that of corresponding materials before sulfidation treatments. This implies the high photocatalytic activity on Co_3S_4/NC@ZnS/NC can be attributed to the synergistic effect of the intrinsic preeminent of the sulfide material itself and the formation of a highly effective heterojunction. In addition, the C_2H_4 selectivity over the various photocatalysts follows the sequence that CoO_x/NC (49.46%) < CoO_x/NC@ZnO/NC (50.11%) < ZnO/NC (56.97%) < ZnS/NC (60.25%) < Co_3S_4/NC (65.91) < Co_3S_4/NC@ZnS/NC (66.99%) (Fig. 4e). The highest activity and selectivity of C_2H_4 indicate that the Co_3S_4/NC@ZnS/NC heterojunction could significantly promote the production of C_2H_4. As illustrated in Fig. S11b and c, both CoO_x/NC@ZnO/NC and Co_3S_4/NC@ZnS/NC maintain relatively stable performance with a slight decrease after five cycles of reaction, which proves the excellent reusability of the catalysts. Besides, the XRD pattern and SEM image of Co_3S_4/NC@ZnS/NC after photocatalytic cycles exhibit no noticeable changes compared to those of the fresh photocatalyst, confirming the good stability of Co_3S_4/NC@ZnS/NC (Fig. S12). In comparison with previously reported heterojunction photocatalysts under gas-solid reaction conditions, Co_3S_4/NC@ZnS/NC shows better catalytic activity and high selectivity for C_2H_4, further indicating the superiority of the combination of Co_3S_4/NC and ZnS/NC (Table S2). The effect of experimental conditions was studied by control experiments(Fig. S11d). The results show that negligible amounts of CO, CH_4 and C_2H_4 are detected without the illumination or photocatalyst, indicating the photocatalytic behavior of the reaction. When CO_2 is replaced with Ar or without the addition of water vapor, almost no gas products can be observed, which suggests that the products originate from the CO_2 with H_2O vapor by photoreduction. The origin of CO_2 photoreduction products are further confirmed by $^{13}CO_2$ labeling experiments. Fig. 4f shows that the signal at $m/z = 17$, 29, 30 and 45 are attributed to $^{13}CH_4$, ^{13}CO, $^{13}C_2H_4$ and $^{13}CO_2$, respectively, demonstrating that CH_4, CO and C_2H_4 are indeed from the C source of CO_2.
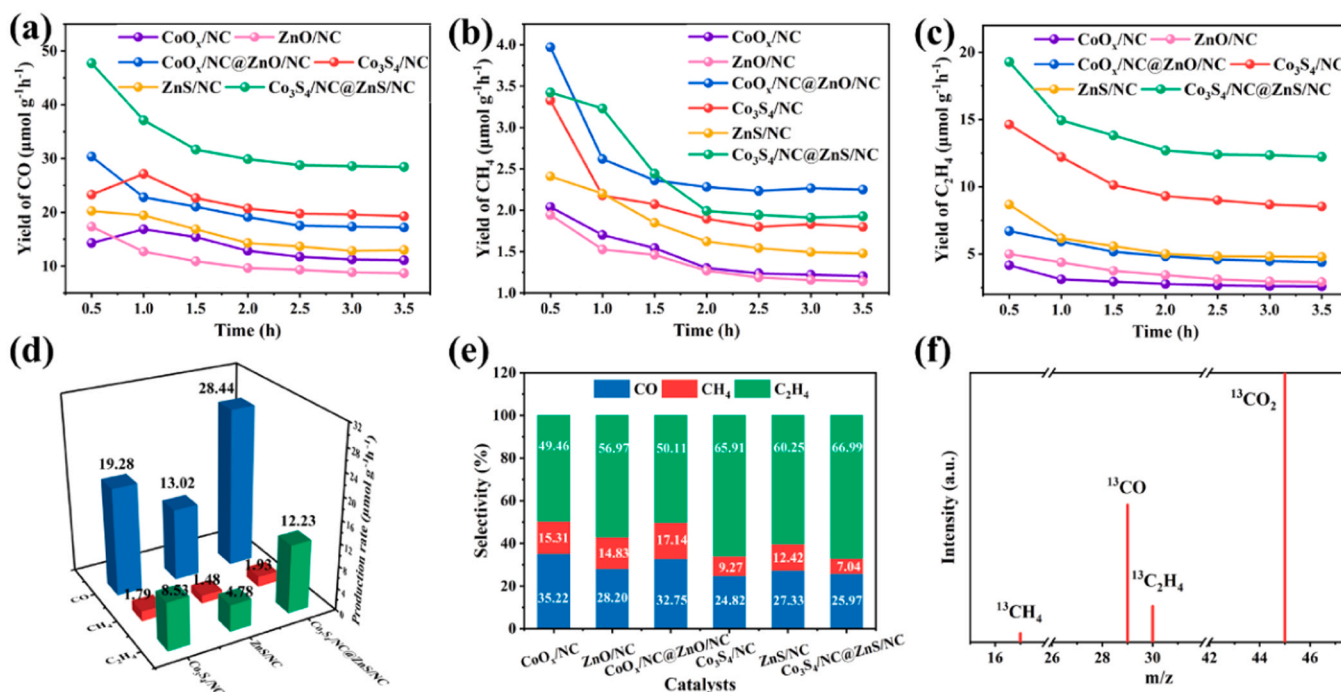

Fig. 4. Production rates of (a) CO, (b) CH_4 and (c) C_2H_4 of CO_2 photoreduction over different samples under visible-light irradiation, (d) the stabilized production rates of Co_3S_4/NC, ZnS/NC and Co_3S_4/NC@ZnS/NC, (e) products selectivity of CO_2 reduction over different samples. (f) GC-MS analysis of photocatalytic $^{13}CO_2$ reduction over Co_3S_4/NC@ZnS/NC.

3.3. CO₂ adsorption behaviors

The specific surface area and corresponding pore size features for the various photocatalysts are shown in Fig. 5a and S13. All the isotherm profiles can be characterized as type IV isotherm models with hysteresis loops, indicating the presence of mesoporous structures. According to Table S3, the BET specific surface areas of CoO_x/NC, $CoO_x/NC@ZnO/NC$, Co_3S_4/NC, ZnS/NC and $Co_3S_4/NC@ZnS/NC$ are calculated to be 32.53, 66.83, 33.82, 165.61 and 121.63 $m^2\,g^{-1}$, respectively. The $CoO_x/NC@ZnO/NC$ reveals a significantly higher BET specific surface area than that of CoO_x/NC, indicating the introduction of ZnO/NC layer may improve the microstructure of the whole sample to enhance the BET specific surface area. The $Co_3S_4/NC@ZnS/NC$ has a higher BET specific surface area than that of Co_3S_4/NC, which can be attributed to the fluffy surface caused by the formation of ZnS/NC on the surface of Co_3S_4/NC. Furthermore, $Co_3S_4/NC@ZnS/NC$ also exhibits much more superior textural properties with a dominant mesopore structure and a considerably high pore volume in comparison with other materials. The above findings indicate that $Co_3S_4/NC@ZnS/NC$ can supply more active sites for reactant adsorption as well as form a satisfying micro-environment for accelerating the mass transfer and charge separation during the reaction [16,44].

Additionally, the $Co_3S_4/NC@ZnS/NC$ possesses the highest CO_2 adsorption capacity with an uptake of 20.1 $cm^3\,g^{-1}$, slightly surpassing that of Co_3S_4/NC (17.7 $cm^3\,g^{-1}$), whereas the CO_2 adsorption capacities of CoO_x/NC and $CoO_x/NC@ZnO/NC$ are only 4.8 and 6.0 $cm^3\,g^{-1}$, respectively (Fig. 5b). This hints that the excellent structural properties resulting from the successful construction of the $Co_3S_4@ZnS/NC$ heterojunction can elevate the CO_2 adsorption. The higher CO_2 adsorption capacity will provide more accessible reactive sites to trigger photocatalytic CO_2 conversion, thus improving the performance of CO_2

photoreduction [4]. Moreover, CO_2--TPD was measured to further study the CO_2 adsorption behaviors. As depicted in Fig. 5c, a wide weak peak at around 114.1 °C corresponds to the desorption of physically-adsorbed CO_2, and all the samples show a comparable physical adsorption of CO_2. The higher peak in the range of 230 ~ 360 °C is ascribed to the desorption of chemisorbed CO_2. In reference to that of CoO_x/NC and ZnO/NC, the Co_3S_4/NC and $Co_3S_4/NC@ZnS/NC$ show a stronger CO_2 chemisorption peak, which demonstrates the sulfurized catalysts have strengthened CO_2 binding affinity. Clearly, $Co_3S_4/NC@ZnS/NC$ displays improved chemisorption of CO_2 compared to Co_3S_4/NC, indicating the presence of more strong-binding sites in heterojunction. DFT calculations were carried out to investigate the adsorption of CO_2 on the surface of various materials (Fig. 5d-f). The optimized stable adsorption configurations show that the CO_2 adsorption energies (E_{ads}) of Co_3S_4/NC and ZnS/NC are −0.16 eV and −0.13 eV, respectively. For $Co_3S_4/NC@ZnS/NC$, the optimal CO_2 adsorption sites are close to the heterojunction interface, in which one C atom and one O atom of CO_2 are preferentially binding with the Co atom and another O atom is binding with the Zn atom. This dual adsorption site configuration results in a substantial increase in E_{ads} to −0.42 eV, illustrating a stronger adsorption capacity for CO_2. The above results indicate that adding the outer surface layer ZnS/NC to form $Co_3S_4/NC@ZnS/NC$ heterojunction is conducive to the adsorption and activation of CO_2.

3.4. Photoelectric properties and band structure analyses

As illustrated in Fig. 6a, the four samples all display two characteristic peaks at about 1325 and 1586 cm^{-1}, which can belong to the D-band and G-band of carbon structure, respectively. The D-band is assigned to structural defects and disordered carbon, while the G-band originates from the ordered graphitic carbon [45]. In comparison with
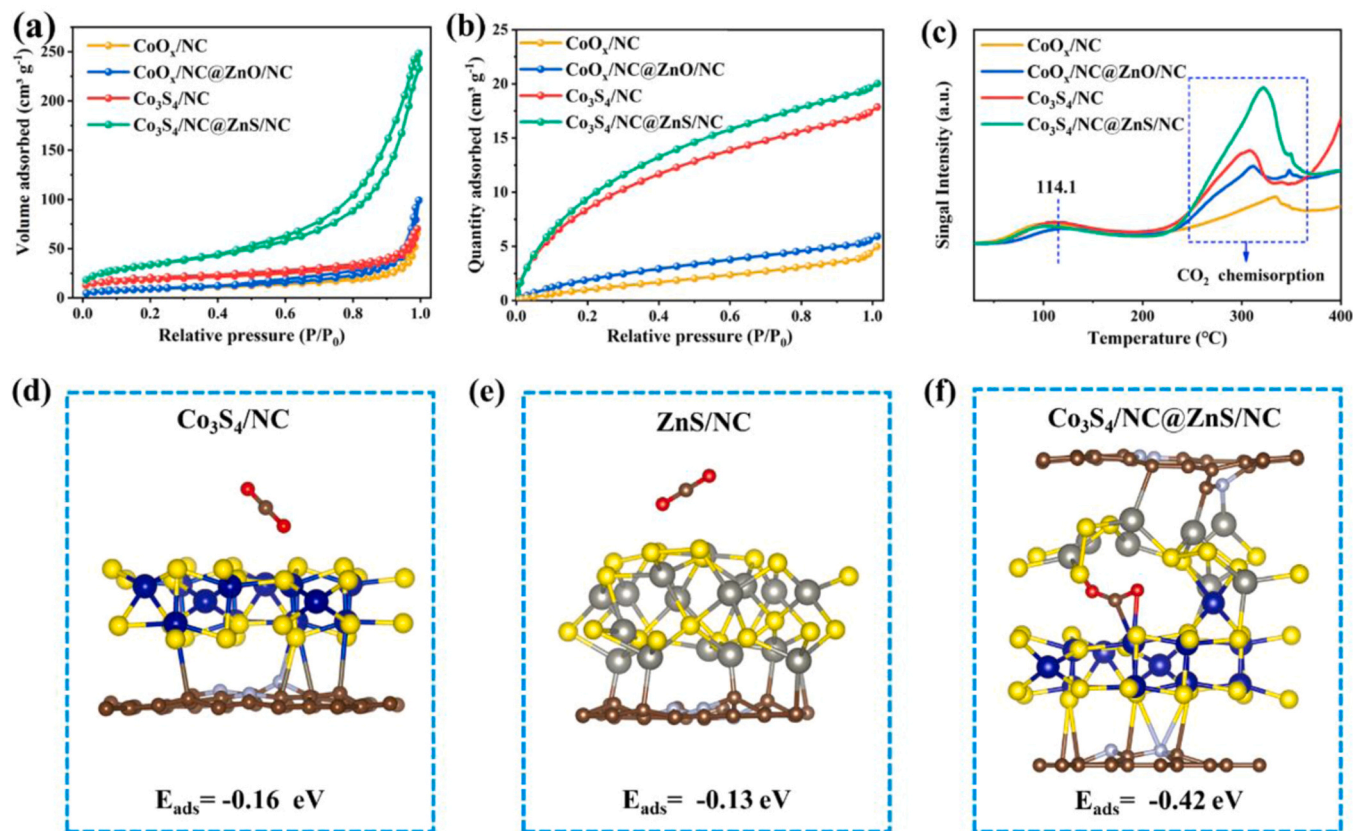

Fig. 5. (a) N_2 adsorption-desorption isotherms (b) CO_2 adsorption isotherms and (c) CO_2-TPD profiles of CoO_x/NC, $CoO_x/NC@ZnO/NC$, Co_3S_4/NC and $Co_3S_4/NC@ZnS/NC$ and the adsorption energies of CO_2 on (d) Co_3S_4/NC, (e) ZnS/NC and (f) $Co_3S_4/NC@ZnS/NC$.
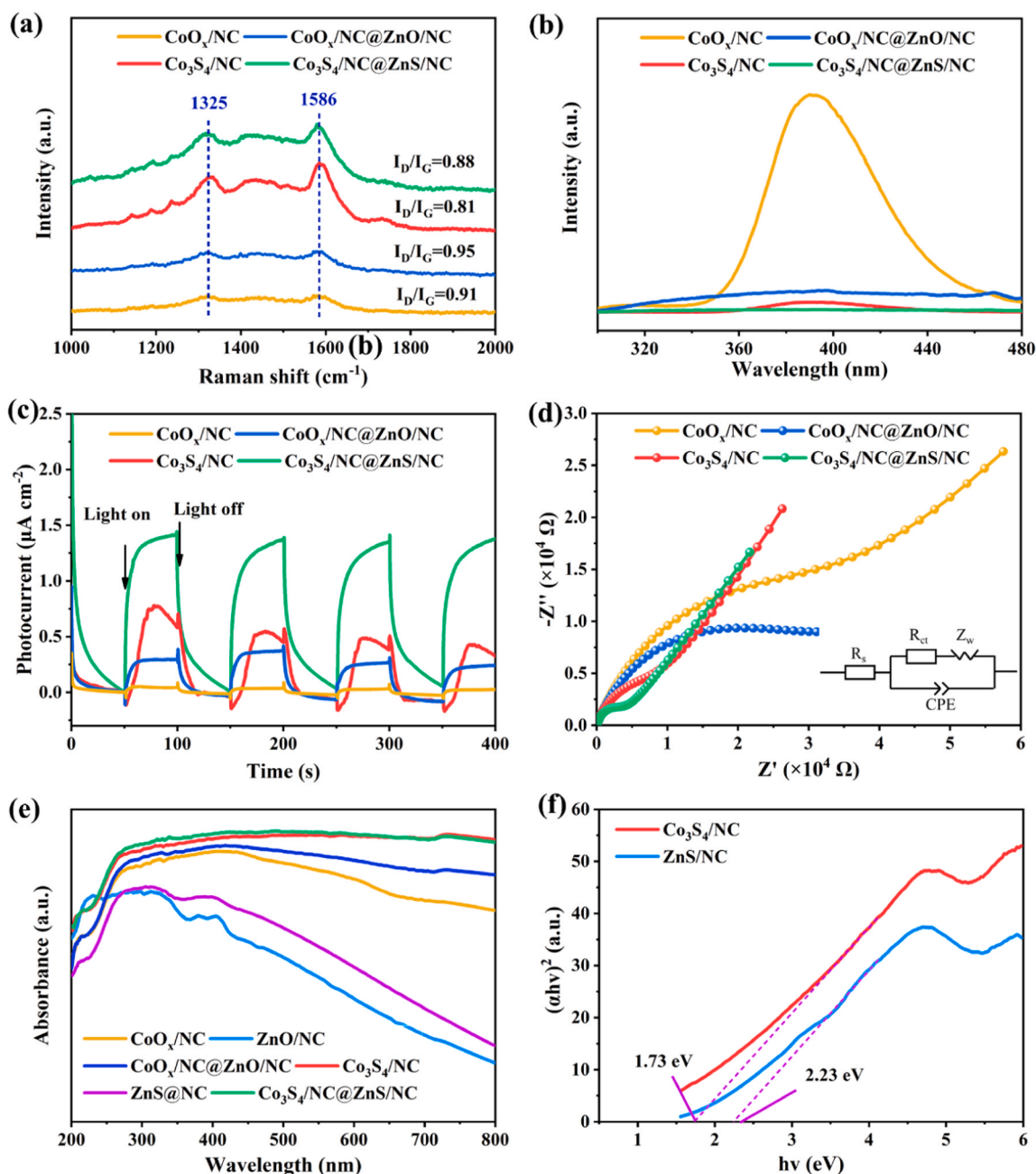
Fig. 6. (a) Raman spectra, (b) steady-state PL spectra, (c) transient photocurrent responses and (d) EIS Nyquist plots of CoO_x/NC, $CoO_x/NC@ZnO/NC$, Co_3S_4/NC and $Co_3S_4/NC@ZnS/NC$, (e) UV–vis DRS of different samples and (f) Tauc plots of Co_3S_4/NC and ZnS/NC.

CoO_x/NC and $CoO_x/NC@ZnO/NC$, the lower I_D/I_G values of Co_3S_4/NC and $Co_3S_4/NC@ZnS/NC$ imply that the sulfidation treatment is conducive to improving the graphitization degree of carbon. Moreover, the values of I_D/I_G reveal a decrease from $Co_3S_4/NC@ZnS/NC$ (0.88) to Co_3S_4/NC (0.81), suggesting that the introduction of ZnS/NC could disrupt the conjugated sp^2 cluster and generate more defects [46]. Notably, the synergistic effect of the appropriate graphitization degrees and structural defects would facilitate electron mobility and further promote the photocatalytic reaction [47,48]. For a better understanding of the photogenerated charge separation and transfer behaviors, steady-state photoluminescence (PL) and photoelectrochemical characterizations were carried out. As presented in Fig. 6b, the PL intensity of $CoO_x/NC@ZnO/NC$ is markedly quenched relative to the intensity of CoO_x, indicating that electron-hole recombination is significantly inhibited. The $Co_3S_4/NC@ZnS/NC$ shows the weakest PL intensity in comparison with other samples, which suggests the efficient photoinduced electron transfer between the Co_3S_4/NC and ZnS/NC [49]. Furthermore, under light irradiation, the photocurrent density follows the order of $CoO_x/NC < CoO_x/NC@ZnO/NC < Co_3S_4/NC < Co_3S_4/NC@ZnS/NC$ (Fig. 6c). The significant increase in photocurrent density further demonstrates that the formation a heterojunction can be beneficial to promoting the transfer and separation of photogenerated carriers [50]. Meanwhile, the results of EIS show that the trend of semicircle radius in the high-frequency region is opposite to that of photocurrent density (Fig. 6d). Among these photocatalysts, the smallest semicircle radius of $Co_3S_4/NC@ZnS/NC$ corresponds to lowest charge transfer resistance, which once again supports the highest efficiency of electron-hole separation and the highest speed of interfacial charge transfer over $Co_3S_4/NC@ZnS/NC$ heterojunction [51]. By combining the photocatalytic performance results, it can be reasonably deduced

that the construction of the heterojunction can effectively improve the separation and transmission of photogenerated carriers, thus rendering the higher activity of CO_2 photoreduction.

The UV–vis DRS was carried out to study the light-harvesting ability of the samples. As observed in Fig. 6e, ZnO/NC exhibits limited light absorption capacity in the visible region, while the CoO_x/NC responds to the light across full spectrum. Evidently, CoO_x/NC@ZnO/NC shows stronger light-harvesting abilities than CoO_x/NC and ZnO/NC, which might be related to the superiority of core-shell structure. Moreover, the absorption edge of ZnS/NC displays a red shift due to the transformation of ZnO into ZnS and the alteration of N-doped carbon skeletons after a sulfidation treatment. The absorption band of Co_3S_4/NC@ZnS/NC is almost identical to that of Co_3S_4/NC, presenting the highest light absorption throughout the entire spectral region. This high light-harvesting ability can lead to significant photothermal effects, thus enhancing charge transfer [18]. Based on the corresponding Tauc plots, the band gap values of Co_3S_4/NC and ZnS/NC are estimated to be 1.73 and 2.23 eV, respectively (Fig. 6f). The Mott-Schottky plots of Co_3S_4/NC and ZnS/NC both show typical n-type characteristics with positive slopes. Moreover, the flat-band potentials (E_{FB}) of Co_3S_4/NC and ZnS/NC are approximately −0.82 and −0.71 V vs. Ag/AgCl, respectively, which correspond to −0.62 and −0.51 V vs. NHE, respectively (Fig. S14). The conduction band (CB) values of n-type semiconductors is considered to be more negative than E_{FB} by about 0.2 V [50,52], thus the CB values of Co_3S_4/NC and ZnS/NC are evaluated to be −0.82 and −0.71 V vs. NHE, respectively. Taking the band gap values into account, the valence band (VB) values of Co_3S_4/NC and ZnS/NC are calculated to be 0.91 and 1.52 V vs. NHE, respectively.

3.5. Theoretical calculation analyses

DFT calculations were utilized to explore the electronic properties of samples as well as deeply inquire into the electron transfer trend at the interface of Co_3S_4/NC@ZnS/NC. The optimized geometric structures of Co_3S_4/NC, ZnS/NC and Co_3S_4/NC@ZnS/NC are displayed in Fig. S15. The energy band diagram of Co_3S_4/NC (Fig. 7a) shows no obvious band gap structure, suggesting the metalloid characteristics [53]. The density

of states (DOS) in Fig. 7d shows that the energy band near the Fermi level of Co_3S_4/NC is mostly contributed by Co-d, S-p and C-p orbitals, and the same phenomenon can be observed in Co_3S_4/NC@ZnS/NC (Fig. 7f). The simulated band gap of ZnS/NC is 0.38 eV, which is identified as a semiconductor (Fig. 7b). Moreover, the primary contributor to the valence band maximum (VBM) in ZnS/NC comes from the C-p orbitals, while the conduction band minimum (CBM) is mainly composed of Zn-d, S-p, and C-p orbitals (Fig. 7e). Due to the interfacial reaction in Co_3S_4/NC@ZnS/NC, more Fermi energy level hybridization can be observed compared to the Co_3S_4/NC and ZnS/NC (Fig. 7c). The dense band distribution in Co_3S_4/NC@ZnS/NC manifests the higher electrical conductivity, which may contribute to migration of electrons during the photocatalytic reaction [54].

The work function (Φ) as a significant parameter for exploring the interfacial charge transfer, is estimated by the energy difference between the potential of vacuum energy and Fermi energy. As displayed in Fig. 8a, b, the Φ of Co_3S_4/NC and ZnS/NC are determined to be 5.18 and 4.89 eV, respectively. Since the Φ value of ZnS/NC is lower than that of Co_3S_4/NC, when ZnS/NC and Co_3S_4/NC come in contact to form a tight interface, the electrons in ZnS/NC will migrate through the contact interface to Co_3S_4/NC until equilibrium of Fermi energy level is reached (Fig. 8e) [55]. During interfacial electron transfer, an upward energy band bending appears in ZnS/NC due to the lost electrons and a downward energy band occurs in Co_3S_4/NC can be attributed to the electron gain. Meanwhile, an internal electric field (IEF) between Co_3S_4/NC and ZnS/NC is formed with the direction from ZnS/NC to Co_3S_4/NC. The simulated charge density difference of Co_3S_4/NC@ZnS/NC (Fig. 8c) exhibits that an electron depletion region represented by cyan color forms on the ZnS/NC side and an electron accumulation region represented by yellow color appears on the Co_3S_4/NC side, which confirms the existence of a IEF at the contact interface [35]. The plane-average electron density difference along the Z direction (Fig. 8d) allows a more intuitive analysis of the charge density in the photocatalyst. In the interfacial region, the negative charge accumulates at the Co_3S_4/NC side, while the positive charge accumulates on the ZnS/NC, which indicates that the electrons pass through the interface from the ZnS/NC to Co_3S_4/NC. This also verifies the charge
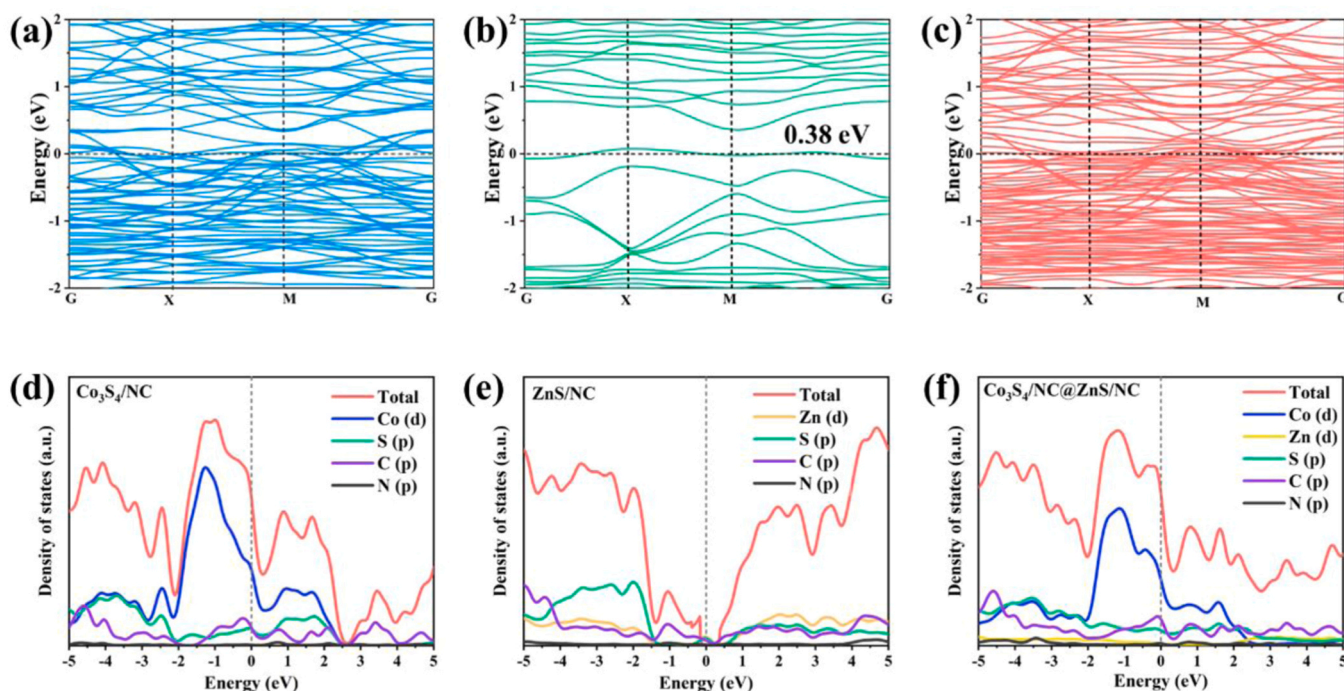

Fig. 7. Calculated band structures of (a) Co_3S_4/NC, (b) ZnS/NC and (c) Co_3S_4/NC@ZnS/NC, calculated density of states (DOS)of (d) Co_3S_4/NC, (e) ZnS/NC and (f) Co_3S_4/NC@ZnS/NC.

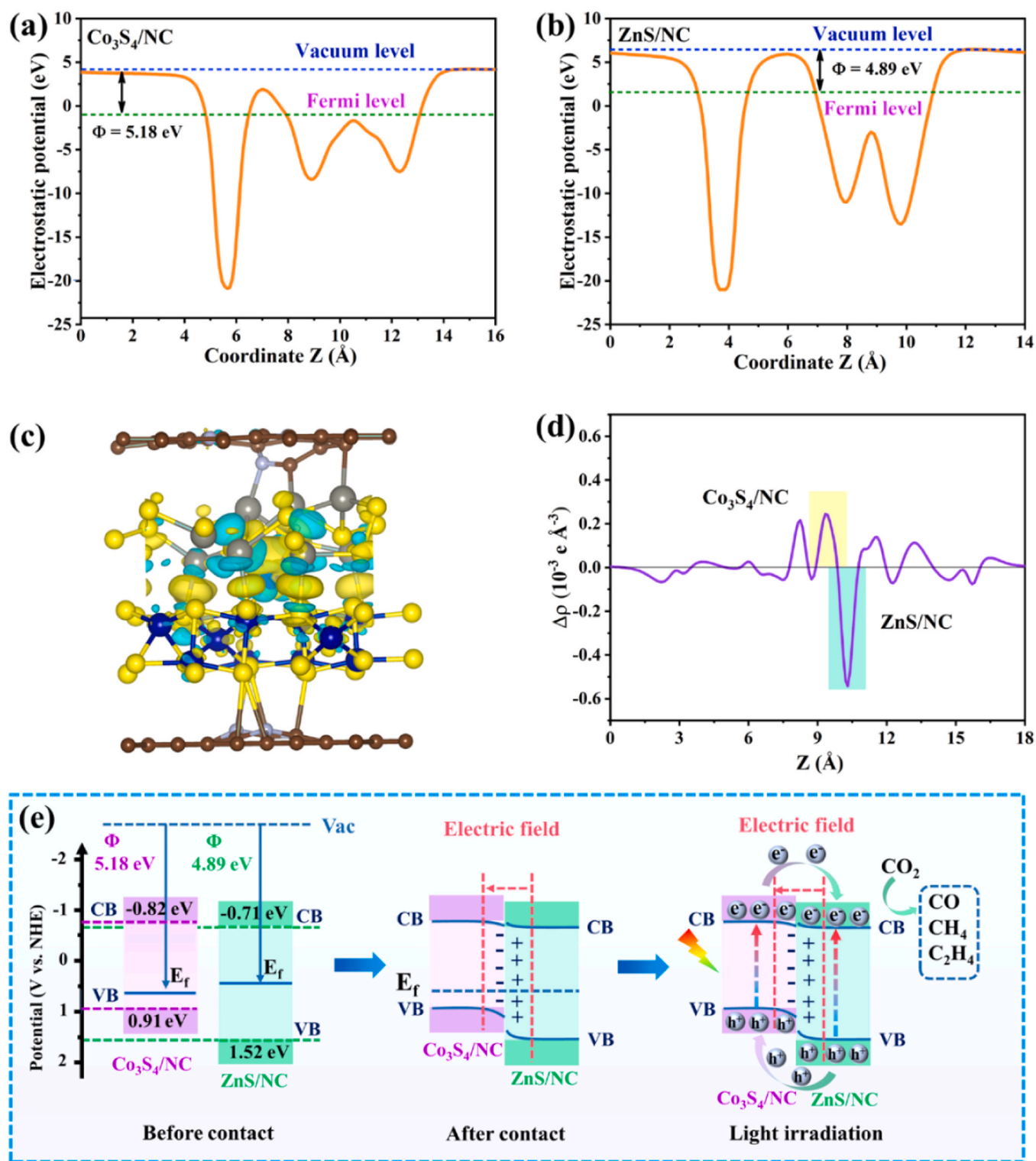**Fig. 8.** The DFT calculated work functions of (a) Co_3S_4/NC and (b) ZnS/NC, (c) the charge density difference and (d) Planar-averaged electron density difference $\Delta\rho(z)$ for Co_3S_4/NC@ZnS/NC, (e) energy band structure, formation of internal electric field and possible photocatalytic charge transfer mechanism of Co_3S_4/NC@ZnS/NC.

redistribution and the charge transfer direction. These charge transfer consequences suggest that outer ZnS/NC serves as an electron transport layer to regulate the electronic structure of the entire catalyst, and further combined with Co_3S_4/NC to generate an available channel for the charge transport process.

Based on the above, a feasible charge migration mechanism over

Co_3S_4/NC@ZnS/NC heterojunction is proposed (Fig. 8e). Upon irradiation, electrons on VB of ZnS/NC and Co_3S_4/NC are excited to respective CB and holes are left on respective VB. Owing to the combined effect of IEF and energy band bending, the photogenerated electrons at the CB of Co_3S_4/NC could spontaneously migrate to the CB of ZnS/NC, while the photogenerated holes at the VB of ZnS/NC easily transfer to the VB of

Co_3S_4/NC. As a result, a typical type-II charge transfer pathway is formed in the n-n heterojunction interface of $Co_3S_4/NC@ZnS/NC$. Importantly, this transfer mechanism would lead to a stronger reduction potential in CB of ZnS/NC, facilitating the reduction of CO_2.

3.6. Photocatalytic CO_2 reduction mechanism

To insight into the evolution of reactive species and possible reaction paths of photocatalytic CO_2 reduction over the $Co_3S_4/NC@ZnS/NC$, in situ DRIFTS was conducted (Figs. 9a and S16a-c). The adsorption peaks in the range of 2300–2400 cm^{-1} correspond to $\nu_3(CO_2)$ absorption of the CO_2 molecular [44], along with the presence of the weak overtone bands of gaseous CO_2 centered at around 3600, 3625, 3705 and 3727 cm^{-1} [56]. In addition, the peak at 1646 cm^{-1} is assigned to the O-H bending vibration of H_2O [57]. Notably, the O-H stretching vibration from H_2O can also be detected in the range of 3550–3750 cm^{-1} [58], which overlaps with the characteristic vibration of adsorbed gas-phase CO_2. The good adsorption of CO_2/H_2O reactants on $Co_3S_4/NC@ZnS/NC$ surface can trigger the CO_2 photoreduction. The absorption peaks at 1472, 1490, and 1543 cm^{-1} are identified as monodentate carbonate (m-CO_3^{2-}) [5,59] and the peak at 1456 cm^{-1} is a sign of bicarbonate (HCO$_3^-$) [60,61]. The appearance of CO_2^- species (1521 cm^{-1}) indicates that the adsorbed CO_2 could be activated on the surface of the photocatalyst [62]. The peaks assigned to formic acid (COOH*) peaks are detected at 1338, 1556, and 1717 cm^{-1} [63–65], which are recognized as a critical intermediate in photocatalytic CO_2 reduction. Moreover, a peak at 2077 cm^{-1} is ascribed to the CO* species [20], while the peaks at 1417 and 1749 cm^{-1} belong to CH$_2$O* [66] and CHO* [67], respectively. Importantly, the peaks positioned at 1371 and 1396 cm^{-1} are associated with CH$_2$* and CH$_3$*, respectively [57]. Besides, the C–H
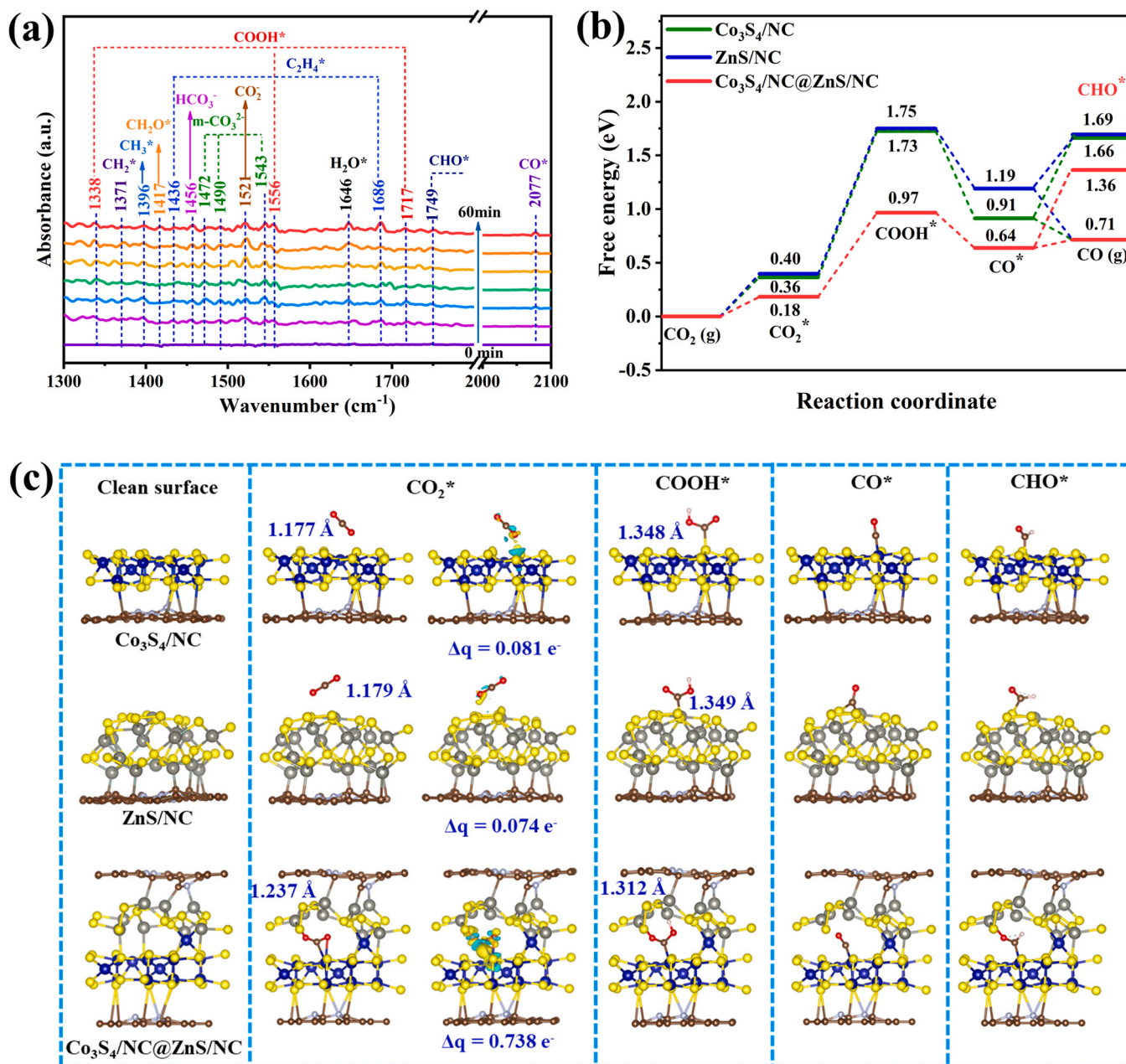

Fig. 9. (a) In situ DRIFTS spectra for the CO_2 photoreduction on $Co_3S_4/NC@ZnS/NC$, (b) free energy diagrams of Co_3S_4/NC, ZnS/NC and $Co_3S_4/NC@ZnS/NC$ for CO_2 photoreduction, (c) simulated configurations of adsorbed intermediates on Co_3S_4/NC, ZnS/NC and $Co_3S_4/NC@ZnS/NC$. (The colors of yellow and cyan represent accumulation and loss of electrons, respectively).

stretching vibrations of CH_2* (2853 and 2921 cm^{-1}) and CH_3* (2890 and 2950 cm^{-1}) are also observed in Fig. S16c [68]. The existence of key CH_x species is directly relevant to the subsequent CH_4 and C_2H_4 products. It should be noted that two peaks centered at 1436 and 1686 cm^{-1} refer to C_2H_4* species [57], providing solid experimental evidence for the formation of C_2H_4.

Combining with the above results, possible CO_2 photoreduction pathways over Co_3S_4/NC@ZnS/NC are put forward in Fig. S16d. Under light irradiation, the Co_3S_4/NC@ZnS/NC is excited to produce abundant photogenerated electrons and holes. The adsorbed CO_2 could rapidly capture photogenerated electrons and be activated into CO_2^- species during the initial period. When these CO_2^- species interact with the protons (H*) derived from water dissociation, the COOH* intermediate gradually appears. Subsequently, a proton-coupled electron transfer step is performed on COOH* to form CO*. Furthermore, it is speculated that the CO* could either be converted into CO molecules through a desorption process or undergo stepwise hydrogenation to generate CHO*, CH_2O*, CH_2* and CH_3* for producing CH_4 and C_2H_4. Specially, the formation of C_2H_4 involves the coupling of CH_2* to obtain C_2H_4* and eventually desorbing to produce C_2H_4.

According to the above experiment results, the Gibbs free energies (ΔG) of Co_3S_4/NC, ZnS/NC and Co_3S_4/NC@ZnS/NC during the reaction process were further investigated by DFT calculations (Fig. 9b). The energy barriers from CO_2 to CO_2* are 0.36 and 0.40 eV over the Co_3S_4/NC and ZnS/NC, respectively, while 0.18 eV over the Co_3S_4/NC@ZnS/NC, which evidences the enhanced adsorption of CO_2 on the Co_3S_4/NC@ZnS/NC surface. The charge density difference reveals that both Co and Zn sites in Co_3S_4/NC@ZnS/NC can inject electrons into CO_2 molecules, thus facilitating a strong interaction between the catalyst surface and CO_2 (Fig. 9c). According to Bader charge analyses, the adsorbed CO_2 species receive the amount of charge from Co_3S_4/NC@ZnS/NC (0.738 e$^-$) is much higher than from Co_3S_4/NC (0.081 e$^-$) and ZnS/NC (0.074 e$^-$), suggesting that the presence of Zn and Co dual-atom pairs within the Co_3S_4/NC@ZnS/NC catalyst punches through the electron transport channels. In addition, compared with Co_3S_4/NC (1.177 Å) and ZnS/NC (1.179 Å), the C–O bond length of the adsorbed CO_2 on Co_3S_4/NC@ZnS/NC (1.237 Å) is markedly prolonged. These findings manifest that the dual Co and Zn active adsorption sites can afford more impressive CO_2 activation ability, which is beneficial for the subsequent generation of intermediates. The energy barrier value of CO_2* to COOH* for Co_3S_4/NC@ZnS/NC (0.79 eV) is much lower than that for Co_3S_4/NC (1.37 eV) and ZnS/NC (1.35 eV), proving that the more efficient activation of CO_2 greatly reduces the difficulty of formation COOH* intermediate. Notably, the rate-limiting step for CO_2 conversion occurs in the formation of COOH* because it requires the highest amount of energy input. The lowest energy barrier in Co_3S_4/NC@ZnS/NC suggests that the introduction of ZnS/NC could promote the kinetics of catalytic reaction, and further results in the highest photocatalytic CO_2 reduction performance. The downhill in free energy changes on the photocatalysts indicates that the transformation from COOH* to CO* could be thermodynamically favorable. Co_3S_4/NC@ZnS/NC has a slightly shorter C−OH bond length, which might make it less prone to breaking the C−OH bond in COOH* to form CO* compared to Co_3S_4/NC and ZnS/NC. However, this seems to have a limited impact on the entire reduction process. Moreover, the energy required for the hydrogenation of CO* to CHO* over three photocatalysts is higher than that required for the desorption of CO* to CO, indicating that the release of CO outweighs the formation of CHO*. It also implies the lower yield of CH_4 and C_2H_4, since the CHO* is the crucial intermediate for the CH_4 and C_2H_4 generation, which agrees well with the experimental results. Based on the simulated adsorbed configurations in Fig. 9c, it can be seen that non-bonding Co and Zn atomic pairs synergistically participate in the activation of CO_2 and the generation of crucial intermediates (COOH*), inducing changes in the lower energy barriers.

4. Conclusions

In summary, a core-shell Co_3S_4/NC@ZnS/NC heterojunction with an outer ZnS/NC electron transport layer has been successfully synthesized through a three-step fabrication procedure, including the formation of MOF-on-MOF precursors (ZIF-67@ZIF-8), the subsequent carbonization and final hydrothermal sulfidation. Compared with Co_3S_4/NC and ZnS/NC, the resultant Co_3S_4/NC@ZnS/NC with distributed Co_3S_4 and ZnS nanoparticles delivers more outstanding photocatalytic performance for converting CO_2 with H_2O vapor into CO (28.44 μmol g^{-1} h^{-1}), CH_4 (1.93 μmol g^{-1} h^{-1}) and C_2H_4 (12.23 μmol g^{-1} h^{-1}) under visible-light irradiation. DFT calculations along with experimental results reveal the electron transfer orientation from ZnS/NC to Co_3S_4/NC, generating an IEF as well as bending the energy bands at interfaces. This promotes the formation of the type II charge transfer pathway in Co_3S_4/NC@ZnS/NC, which can provide a good channel for enhancing the charge separation and transfer, and thus effectively promote the CO_2 reduction on Co_3S_4/NC. Moreover, the synergistic effect of the bimetallic sulfide composition, core-shell structure, and carbon-doped nitrogen matrix can lead to sufficient active sites, enhanced light absorption capacity and rich sulfur vacancies, improving the photocatalytic activity. The results of in situ DRIFTS show that the product of gaseous CO is derived from the desorption of CO* intermediate, while the formation of CH_4 and C_2H_4 may be attributed to the multi-step hydrogenation of CO* intermediate. DFT calculations also reveal the strong interaction between dual-active sites (Co and Zn) and CO_2 molecules improves the CO_2 activation and synergistically facilitates the formation of COOH*, thereby encouraging the generation of reduction products. Our finding might provide a MOF-on-MOF strategy to develop core-shell dual-metal sulfide heterojunction catalysts with a valid electron transport layer for efficient light-driven CO_2 reduction to C_2 hydrocarbon and is expected to be extended to the design of other photocatalysts with reinforced properties.

CRediT authorship contribution statement

Lili Huang: Writing – original draft, Methodology, Investigation, Formal analysis, Data curation, Conceptualization. **Shengpeng Mo:** Writing – review & editing, Methodology, Funding acquisition, Data curation, Conceptualization. **Xin Zhao:** Validation, Methodology, Investigation. **Jiangjing Zhou:** Visualization, Validation, Investigation. **Xiaobin Zhou:** Visualization, Investigation. **Yanan Zhang:** Writing – review & editing, Validation, Funding acquisition, Investigation. **Yinming Fan:** Validation, Investigation. **Qinglin Xie:** Supervision, Investigation, Funding acquisition. **Bing Li:** Validation, Investigation. **Junhua Li:** Writing – review & editing, Validation, Investigation.

Declaration of Competing Interest

The authors declared that they have no conflicts of interest to this work. We declare that we do not have any commercial or associative interest that represents a conflict of interest in connection with the work submitted.

Data availability

Data will be made available on request.

Acknowledgement

Engineering (MESO-23-D11).

Appendix A. Supporting information

Supplementary data associated with this article can be found in the online version at doi:10.1016/j.apcatb.2024.124019.

References

[1] J. Wang, S. Lin, N. Tian, T. Ma, Y. Zhang, H. Huang, Nanostructured metal sulfides: classification, modification strategy, and solar-driven CO_2 reduction application, Adv. Funct. Mater. 31 (2020) 2008008, https://doi.org/10.1002/adfm.202008008.

[2] F.O. Ochedi, D. Liu, J. Yu, A. Hussain, Y. Liu, Photocatalytic, electrocatalytic and photoelectrocatalytic conversion of carbon dioxide: a review, Environ. Chem. Lett. 19 (2020) 941–967, https://doi.org/10.1007/s10311-020-01131-5.

[3] Q. Liu, J. Lin, H. Cheng, L. Wei, F. Wang, Simultaneous co-photocatalytic CO_2 reduction and ethanol oxidation towards synergistic acetaldehyde synthesis, Angew. Chem. Int. Ed. 62 (2023) 202218720, https://doi.org/10.1002/anie.202218720.

[4] H. Yang, D. Zhang, Y. Luo, W. Yang, X. Zhan, W. Yang, H. Hou, Highly efficient and selective visible-light driven photoreduction of CO_2 to CO by metal-organic frameworks-derived Ni-Co-O porous microrods, Small 18 (2022) 2202939, https://doi.org/10.1002/smll.202202939.

[5] W. Xie, K. Li, X.H. Liu, X. Zhang, H. Huang, P-mediated Cu–N_4 sites in carbon nitride realizing CO_2 photoreduction to C_2H_4 with selectivity modulation, Adv. Mater. 35 (3) (2022) 202208132, https://doi.org/10.1002/adma.20220813.

[6] G. Yin, X. Qi, Y. Chen, C. Peng, X. Jiang, Q. Wang, W. Zhang, X. Gong, Constructing an all zero-dimensional $CsPbBr_3$/CdSe heterojunction for highly efficient photocatalytic CO_2 reduction, J. Mater. Chem. A 10 (2022) 22468–22476, https://doi.org/10.1039/d2ta05186a.

[7] D. Li, M. Kassymova, X. Cai, S.Q. Zang, H.L. Jiang, Photocatalytic CO_2 reduction over metal-organic framework-based materials, Coord. Chem. Rev. 412 (2020) 213262, https://doi.org/10.1016/j.ccr.2020.213262.

[8] X. Lin, Z. Xie, B. Su, M. Zheng, W. Dai, Y. Hou, Z. Ding, W. Lin, Y. Fang, S. Wang, Well-defined Co_9S_8 cages enable the separation of photoexcited charges to promote visible-light CO_2 reduction, Nanoscale 13 (2021) 18070–18076, https://doi.org/10.1039/d1nr04812k.

[9] X. Jiao, Z. Chen, X. Li, Y. Sun, S. Gao, W. Yan, C. Wang, Q. Zhang, Y. Lin, Y. Luo, Y. Xie, Defect-mediated electron–hole separation in one-unit-cell $ZnIn_2S_4$ layers for boosted solar-driven CO_2 reduction, J. Am. Chem. Soc. 139 (2017) 7586–7594, https://doi.org/10.1021/jacs.7b02290.

[10] X. Jiao, X. Li, X. Jin, Y. Sun, J. Xu, L. Liang, H. Ju, J. Zhu, Y. Pan, W. Yan, Y. Lin, Y. Xie, Partially oxidized SnS_2 atomic layers achieving efficient visible-light-driven CO_2 reduction, J. Am. Chem. Soc. 13 (2017) 18044–18051, https://doi.org/10.1021/jacs.7b10287.

[11] H. Pang, X. Meng, P. Li, K. Chang, W. Zhou, X. Wang, X. Zhang, W. Jevasuwan, N. Fukata, D. Wang, J. Ye, Cation vacancy-initiated CO_2 photoreduction over ZnS for efficient formate production, ACS Energy Lett. 4 (2019) 1387–1393, https://doi.org/10.1021/acsenergylett.9b00711.

[12] S. Sun, Q. An, M. Watanabe, J. Cheng, H. Ho Kim, T. Akbay, A. Takagaki, T. Ishihara, Highly correlation of CO_2 reduction selectivity and surface electron accumulation: a case study of $Au-MoS_2$ and $Ag-MoS_2$ catalyst, Appl. Catal. B Environ. 271 (2020) 118931, https://doi.org/10.1016/j.apcatb.2020.118931.

[13] S. Li, H. Rui, T. Bao, Y. Qi, H. Rao, P. She, J.-s Qin, Efficient visible-light-driven CO_2 reduction into tunable syngas by cobalt phthalocyanine modified flower-like $ZnIn_2S_4$ nanosheets, Appl. Surf. Sci. 641 (2023) 158492, https://doi.org/10.1016/j.apsusc.2023.158492.

[14] Y. Zhu, J. Ren, G. Huang, C.L. Dong, Y.C. Huang, P. Lu, H. Tang, Y. Liu, S. Shen, D. Yang, Red phosphorus grafted high-index (116) faceted anatase TiO_2 for Z-scheme photocatalytic pure water splitting, Adv. Funct. Mater. 34 (2023) 2311623, https://doi.org/10.1002/adfm.202311623.

[15] P. Lu, K. Liu, Y. Liu, Z. Ji, X. Wang, B. Hui, Y. Zhu, D. Yang, L. Jiang, Heterostructure with tightly-bound interface between In_2O_3 hollow fiber and $ZnIn_2S_4$ nanosheet toward efficient visible light driven hydrogen evolution, Appl. Catal. B Environ. 345 (2024) 123697, https://doi.org/10.1016/j.apcatb.2024.123697.

[16] Y. Zhang, Y. Wu, L. Wan, H. Ding, H. Li, X. Wang, W. Zhang, Hollow core–shell Co_9S_8@$ZnIn_2S_4$/CdS nanoreactor for efficient photothermal effect and CO_2 photoreduction, Appl. Catal. B Environ. 311 (2022) 121255, https://doi.org/10.1016/j.apcatb.2022.121255.

[17] Y. Zhao, Y. Chen, L. Du, Q. Wang, X. Liu, L. Li, G. Tian, Fabrication of size-controlled hierarchical ZnS@$ZnIn_2S_4$ heterostructured cages for enhanced gas-phase CO_2 photoreduction, J. Colloid Interface Sci. 605 (2022) 253–262, https://doi.org/10.1016/j.jcis.2021.07.093.

[18] W. Han, Y. Chen, Y. Jiao, S. Liang, W. Li, G. Tian, ZIF-derived frame-in-cage hybrids of ZnSe–CdSe embedded within a N-doped carbon matrix for efficient photothermal conversion of CO_2 into fuel, J. Mater. Chem. A 10 (2022) 17642–17651, https://doi.org/10.1039/d2ta03219h.

[19] Q. Shen, S. Zhou, F.-L. Yang, X. Wang, X. Han, Engineering one-dimensional hollow beta-In_2S_3/In_2O_3 hexagonal micro-tubes for efficient broadband-light photocatalytic performance, J. Mater. Chem. A 10 (2022) 4974–4980, https://doi.org/10.1039/d2ta00083k.

[20] J. Wang, K. Sun, D. Wang, X. Niu, Z. Lin, S. Wang, W. Yang, J. Huang, H.-L. Jiang, Precise regulation of the coordination environment of single Co(II) sites in a metal–organic framework for boosting CO_2 photoreduction, ACS Catal. 13 (2023) 8760–8769, https://doi.org/10.1021/acscatal.3c01003.

[21] L. Chai, J. Pan, Y. Hu, J. Qian, M. Hong, Rational design and growth of MOF-on-MOF heterostructures, Small 17 (2021) 2100607, https://doi.org/10.1002/smll.202100607.

[22] Y. Pan, K. Sun, S. Liu, X. Cao, K. Wu, W.-C. Cheong, Z. Chen, Y. Wang, Y. Li, Y. Liu, D. Wang, Q. Peng, C. Chen, Y. Li, Core–shell ZIF-8@ZIF-67-derived CoP nanoparticle-embedded N-doped carbon nanotube hollow polyhedron for efficient overall water splitting, J. Am. Chem. Soc. 140 (2018) 2610–2618, https://doi.org/10.1021/jacs.7b12420.

[23] Z. Qin, L. Chen, Y. Li, K. Shen, Bifunctional catalysts with core–shell distributed ZrO_2 and Co nanoparticles derived from MOF-on-MOF heterostructures for economical one-pot tandem CO_2 fixation, ACS Catal. 13 (2023) 8372–8383, https://doi.org/10.1021/acscatal.3c01604.

[24] L. Huang, S. Mo, X. Zhao, J. Zhou, X. Zhou, Y. Zhang, M. Fu, Y. Fan, Q. Xie, D. Ye, Y. Chen, Designing multi-layered MOF-on-MOF-transformed core double-shell FeS_x@ZnS@CoS_x heterojunction for enhanced CO_2 photoreduction with water vapor, Chem. Eng. J. 474 (2023) 145740, https://doi.org/10.1016/j.cej.2023.145740.

[25] J. Li, L. Liu, Q. Liang, M. Zhou, C. Yao, S. Xu, Z. Li, Core-shell ZIF-8@MIL-68(In) derived ZnO nanoparticles-embedded In_2O_3 hollow tubular with oxygen vacancy for photocatalytic degradation of antibiotic pollutant, J. Hazard. Mater. 414 (2021) 125395, https://doi.org/10.1016/j.jhazmat.2021.125395.

[26] H. Zhu, J. Liang, X. Jiao, R. Fu, Q. Jiao, C. Feng, H. Li, Y. Zhang, Y. Zhao, MOF-derived core-shell structured Cu_9S_5/NC@Co_3S_4/NC composite as a high-efficiency electromagnetic wave absorber, Ceram. Int. 49 (2023) 9534–9542, https://doi.org/10.1016/j.ceramint.2022.11.120.

[27] R. Yang, X. Yan, Y. Li, X. Zhang, J. Chen, Nitrogen-doped porous carbon-ZnO nanopolyhedra derived from ZIF-8: new materials for photoelectrochemical biosensors, ACS Appl. Mater. Interfaces 9 (2017) 42482–42491, https://doi.org/10.1021/acsami.7b10856.

[28] J. Shi, J. Xiong, L. Qiao, C. Liu, Y. Zeng, Facile MOF-on-MOF isomeric strategy for ZnO@Co_3O_4 single-shelled hollow cubes with high toluene detection capability, Appl. Surf. Sci. 609 (2023) 155271, https://doi.org/10.1016/j.apsusc.2022.155271.

[29] Y. Xu, J. Long, L. Tu, W. Dai, L. Yang, J. Zou, X. Luo, S. Luo, CoO engineered Co_9S_8 catalyst for CO_2 photoreduction with accelerated electron transfer endowed by the built-in electric field, Chem. Eng. J. 426 (2021) 131849, https://doi.org/10.1016/j.cej.2021.131849.

[30] Y. Yu, S. You, J. Du, Z. Xing, Y. Dai, H. Chen, Z. Cai, N. Ren, J. Zou, ZIF-67-derived CoO (tetrahedral Co^{2+})@nitrogen-doped porous carbon protected by oxygen vacancies-enriched SnO_2 as highly active catalyst for oxygen reduction and Pt co-catalyst for methanol oxidation, Appl. Catal. B-Environ. 259 (2019) 118043, https://doi.org/10.1016/j.apcatb.2019.118043.

[31] F. Wei, X. Zhang, J. Liao, J. Guo, W. Bao, L. Chang, Desulfurization mechanism of an excellent Cu/ZnO sorbent for ultra-deep removal of thiophene in simulated coke oven gas, Chem. Eng. J. 446 (2022) 37140, https://doi.org/10.1016/j.cej.2022.137140.

[32] J. Qiu, W. Zheng, R. Yuan, C. Yue, D. Li, F. Liu, J. Zhu, A novel 3D nanofibrous aerogel-based MoS_2@Co_3S_4 heterojunction photocatalyst for water remediation and hydrogen evolution under simulated solar irradiation, Appl. Catal. B-Environ. 264 (2020) 118514, https://doi.org/10.1016/j.apcatb.2019.118514.

[33] Z. Zhang, Y. Huang, X. Liu, C. Chen, Z. Xu, P. Liu, Zeolitic imidazolate frameworks derived ZnS/Co_3S_4 composite nanoparticles doping on polyhedral carbon framework for efficient lithium/sodium storage anode materials, Carbon 157 (2020) 244–254, https://doi.org/10.1016/j.carbon.2019.10.052.

[34] K. Yang, G. Song, Y. Li, Q. An, S. Zhai, Z. Xiao, Transforming in-situ grown chitosan/ZIF-67 aerogels into 3D N-doped Co/CoO/carbon composites for improved electromagnetic wave absorption, J. Alloy. Compd. 936 (2023) 168195, https://doi.org/10.1016/j.jallcom.2022.168195.

[35] J. Zhu, Q. Bi, Y. Tao, W. Guo, J. Fan, Y. Min, G. Li, Mo-modified $ZnIn_2S_4$@$NiTiO_3$ S-scheme heterojunction with enhanced interfacial electric field for efficient visible-light-driven hydrogen evolution, Adv. Funct. Mater. 33 (2023) 213131, https://doi.org/10.1002/adfm.202213131.

[36] Y. Zhang, J. Wu, S. Zhang, N. Shang, X. Zhao, S.M. Alshehri, T. Ahamad, Y. Yamauchi, X. Xu, Y. Bando, MOF-on-MOF nanoarchitectures for selectively functionalized nitrogen-doped carbon-graphitic carbon/carbon nanotubes heterostructure with high capacitive deionization performance, Nano Energy 97 (2022) 107146, https://doi.org/10.1016/j.nanoen.2022.107146.

[37] W. Qu, Z. Tang, H. Wen, M. Luo, T. Zhong, Q. Lian, L. Hu, S. Tian, C. He, D. Shu, Electron transfer trade-offs in MOF-derived cobalt-embedded nitrogen-doped carbon nanotubes boost catalytic ozonation for gaseous sulfur-containing VOC elimination, ACS Catal. 13 (2022) 692–705, https://doi.org/10.1021/acscatal.2c05285.

[38] Z. Tan, Z. Zhang, Z. Lei, L. Yu, W. Wu, Z. Wang, N. Cheng, Electronic modulation optimizes OH* intermediate adsorption on Co-N_x-C sites via coupling CoNi alloy in hollow carbon nanopolyhedron toward efficient reversible oxygen electrocatalysis, Appl. Catal. B-Environ. 304 (2022) 121006, https://doi.org/10.1016/j.apcatb.2021.121006.

[39] X. Jin, Y. Zhang, J. Huang, L. Xu, Q. Shen, C. Sun, Selective C-Br bond activation for decabromodiphenyl ether photo-debromination via sulfur vacancies enriched zinc indium sulfides, Appl. Surf. Sci. 615 (2023) 156409, https://doi.org/10.1016/j.apsusc.2023.156409.

[40] T. Tian, X. Jin, N. Guo, H. Li, Y. Han, Y. Yuan, CdS/ethylenediamine nanowires 3D photocatalyst with rich sulfur vacancies for efficient syngas production from CO_2 photoreduction, Appl. Catal. B-Environ. 308 (2022) 121227, https://doi.org/10.1016/j.apcatb.2022.121227.

[41] Y. Liu, Y. Zhou, X. Zhou, X. Jin, B. Li, J. Liu, G. Chen, Cu doped SnS_2 nanostructure induced sulfur vacancy towards boosted photocatalytic hydrogen evolution, Chem. Eng. J. 407 (2021) 127180, https://doi.org/10.1016/j.cej.2020.127180.

[42] Z. Niu, X. Gao, S. Lou, N. Wen, J. Zhao, Z. Zhang, Z. Ding, R. Yuan, W. Dai, J. Long, Theory-guided S-defects boost selective conversion of CO_2 to HCOOH over In_4SnS_8 nanoflowers, ACS Catal. 13 (2023) 2998–3006, https://doi.org/10.1021/acscatal.2c05957.

[43] S. Cao, Y. Wang, B. Zhu, G. Xie, J. Yu, J.R. Gong, Enhanced photochemical CO_2 reduction in the gas phase by graphdiyne, J. Mater. Chem. A 8 (2020) 7671–7676, https://doi.org/10.1039/d0ta02256j.

[44] Y. Wang, Z. Hu, W. Wang, Y. Li, H. He, L. Deng, Y. Zhang, J. Huang, N. Zhao, G. Yu, Y.-N. Liu, Rational design of defect metal oxide/covalent organic frameworks Z-scheme heterojunction for photoreduction CO_2 to CO, Appl. Catal. B-Environ. 327 (2023) 122419, https://doi.org/10.1016/j.apcatb.2023.122419.

[45] S. Qiu, T. Gao, H. He, X. Zhao, Z.-H. Liu, Solid CoZn glycerate template-based engineering of yolk-shell bimetallic sulfides heterostructures microspheres confined in N, S-doped carbon as anode materials for lithium/sodium-ion batteries, J. Alloy. Compd. 902 (2022) 163631, https://doi.org/10.1016/j.jallcom.2022.163631.

[46] Y. Liu, S. Fan, Y. Chen, J. Chen, J. Meng, M. Yang, C. Li, H. Qing, Z. Xiao, Catalytic membrane nano reactor with two-dimensional channels assembly of graphene oxide nanosheets with ZIF-67 derived Co_3S_4 catalyst immobilized on, Sep. Purif. Technol. 299 (2022) 121797, https://doi.org/10.1016/j.seppur.2022.121797.

[47] L. Wu, Y. Li, B. Zhou, J. Liu, D. Cheng, S. Guo, K. Xu, C. Yuan, M. Wang, G.J. Hong Melvin, J. Ortiz-Medina, S. Ali, T. Yang, Y.A. Kim, Z. Wang, Vertical graphene on rice-husk-derived SiC/C composite for highly selective photocatalytic CO_2 reduction into CO, Carbon 207 (2023) 36–48, https://doi.org/10.1016/j.carbon.2023.03.003.

[48] W. Zhang, P. Zhang, F. Li, M. He, A. Gong, W. Zhang, X. Mo, K. Li, From MOF to Al/N-doped porous carbon: creating multiple capture sites for efficient capacitive deionization defluorination, Desalination 543 (2022) 116090, https://doi.org/10.1016/j.desal.2022.116090.

[49] L. Wang, B. Cheng, L. Zhang, J. Yu, In situ irradiated XPS investigation on S-scheme $TiO_2@ZnIn_2S_4$ photocatalyst for efficient photocatalytic CO_2 reduction, Small 17 (2021) 2103447, https://doi.org/10.1002/smll.202103447.

[50] J. Liang, H. Yu, J. Shi, B. Li, L. Wu, M. Wang, Dislocated bilayer MOF enables high-selectivity photocatalytic reduction of CO_2 to CO, Adv. Mater. 35 (2023) 2209814, https://doi.org/10.1002/adma.202209814.

[51] N.-Y. Huang, J.-Q. Shen, X.-W. Zhang, P.-Q. Liao, J.-P. Zhang, X.-M. Chen, Coupling ruthenium bipyridyl and cobalt imidazolate units in a metal–organic framework for an efficient photosynthetic overall reaction in diluted CO_2, J. Am. Chem. Soc. 144 (2022) 8676–8682, https://doi.org/10.1021/jacs.2c01640.

[52] Y. Wang, Y. Zeng, S. Wan, S. Zhang, Q. Zhong, Construction of octahedral $BiFeWO_x$ encapsulated in hierarchical In_2S_3 core@shell heterostructure for visible-light-driven CO_2 reduction, J. CO_2 Util. 29 (2019) 156–162, https://doi.org/10.1016/j.jcou.2018.12.009.

[53] J. Li, M. Li, Z. Jin, ZIF-67 derived hierarchical hollow $Co_3S_4@Mo_2S_3$ dodecahedron with an S-scheme surface heterostructure for efficient photocatalytic hydrogen evolution, Catal. Sci. Technol. 12 (2022) 1144–1158, https://doi.org/10.1039/d1cy01757h.

[54] Y. Xiao, B. Yao, M. Cao, Y. Wang, Super-photothermal effect-mediated fast reaction kinetic in S-scheme organic/inorganic heterojunction hollow spheres toward

[55] optimized photocatalytic performance, Small 19 (2023) 202207499, https://doi.org/10.1002/smll.202207499.

[55] M. Dai, H. Yu, W. Chen, K.-A. Qu, D. Zhai, C. Liu, S. Zhao, S. Wang, Z. He, Boosting photocatalytic activity of $CdLa_2S_4/ZnIn_2S_4$ S-scheme heterojunctions with spatial separation of photoexcited carries, Chem. Eng. J. 470 (2023) 144240, https://doi.org/10.1016/j.cej.2023.144240.

[56] Y. Gu, J. Ding, X. Tong, H. Yao, R. Yang, Q. Zhong, Photothermal catalyzed hydrogenation of carbon dioxide over porous nanosheet Co_3O_4, J. CO_2 Util. 61 (2022) 102003, https://doi.org/10.1016/j.jcou.2022.102003.

[57] Y. Yu, X. Dong, P. Chen, Q. Geng, H. Wang, J. Li, Y. Zhou, F. Dong, Synergistic effect of Cu single atoms and Au-Cu alloy nanoparticles on TiO_2 for efficient CO_2 photoreduction, ACS Nano 15 (2021) 14453–14464, https://doi.org/10.1021/acsnano.1c03961.

[58] J. Wu, K. Li, S. Yang, C. Song, X. Guo, In-situ construction of $BiOBr/Bi_2WO_6$ S-scheme heterojunction nanoflowers for highly efficient CO_2 photoreduction: regulation of morphology and surface oxygen vacancy, Chem. Eng. J. 452 (2023) 139493, https://doi.org/10.1016/j.cej.2022.139493.

[59] R. Niu, Q. Liu, B. Huang, Z. Liu, W. Zhang, Z. Peng, Z. Wang, Y. Yang, Z. Gu, J. Li, Black phosphorus/$Bi_{19}Br_3S_{27}$ van der Waals heterojunctions ensure the supply of activated hydrogen for effective CO_2 photoreduction, Appl. Catal. B-Environ. 317 (2022) 121727, https://doi.org/10.1016/j.apcatb.2022.121727.

[60] X.-X. Li, L. Zhang, L. Yuan, T. Wang, L.-Z. Dong, K. Huang, J. Liu, Y.-Q. Lan, Constructing crystalline redox catalyst to achieve efficient CO_2 photoreduction reaction in water vapor, Chem. Eng. J. 442 (2022) 136157, https://doi.org/10.1016/j.cej.2022.136157.

[61] C. Ban, Y. Duan, Y. Wang, J. Ma, K. Wang, J. Meng, X. Liu, C. Wang, X. Han, G. Cao, L. Gan, X. Zhou, Isotype heterojunction-boosted CO_2 photoreduction to CO, Nanomicro Lett. 14 (2022) 74, https://doi.org/10.1007/s40820-022-00821-9.

[62] M. Ma, Z. Huang, L. Li, W. Zhang, R. Guo, R. Zhang, W. Fa, C. Han, Y. Cao, S. Yu, Y. Zhou, Modulating photogenerated electron density of Pr single-atom sites by coordination environment engineering for boosting photoreduction of CO_2 to CH_3OH, Appl. Catal. B-Environ. 330 (2023) 122626, https://doi.org/10.1016/j.apcatb.2023.122626.

[63] X. Yang, X. Lan, Y. Zhang, H. Li, G. Bai, Rational design of $MoS_2@COF$ hybrid composites promoting C-C coupling for photocatalytic CO_2 reduction to ethane, Appl. Catal. B-Environ. 325 (2023) 122393, https://doi.org/10.1016/j.apcatb.2023.122393.

[64] J. Sheng, Y. He, M. Huang, C. Yuan, S. Wang, F. Dong, Frustrated Lewis pair sites boosting CO_2 photoreduction on Cs_2CuBr_4 perovskite quantum dots, ACS Catal. 12 (2022) 2915–2926, https://doi.org/10.1021/acscatal.2c00037.

[65] Y. Li, Z. Ren, M. Gu, Y. Duan, W. Zhang, K. Lv, Synergistic effect of interstitial C doping and oxygen vacancies on the photoreactivity of TiO_2 nanofibers towards CO_2 reduction, Appl. Catal. B-Environ. 317 (2022) 121773, https://doi.org/10.1016/j.apcatb.2022.121773.

[66] G. Feng, S. Wang, S. Li, R. Ge, X. Feng, J. Zhang, Y. Song, X. Dong, J. Zhang, G. Zeng, Q. Zhang, G. Ma, Y.D. Chuang, X. Zhang, J. Guo, Y. Sun, W. Wei, W. Chen, Highly selective photoelectroreduction of carbon dioxide to ethanol over graphene/silicon carbide composites, Angew. Chem. Int. Ed. 62 (2023) 202218664, https://doi.org/10.1002/anie.202218664.

[67] Y.J. Wang, G.L. Zhuang, J.W. Zhang, F. Luo, X. Cheng, F.L. Sun, S.S. Fu, T.B. Lu, Z.M. Zhang, Co-dissolved isostructural polyoxovanadates to construct single-atom-site catalysts for efficient CO_2 photoreduction, Angew. Chem. Int. Ed. 62 (2022) 202216592, https://doi.org/10.1002/anie.202216592.

[68] J. Ma, K. Mao, J. Low, Z. Wang, D. Xi, W. Zhang, H. Ju, Z. Qi, R. Long, X. Wu, L. Song, Y. Xiong, Efficient photoelectrochemical conversion of methane into ethylene glycol by WO_3 nanobar arrays, Angew. Chem. Int. Ed. 60 (2021) 9357–9361, https://doi.org/10.1002/anie.202101701.